Cell Reports

Article

Fortuitous somatic mutations during antibody evolution endow broad neutralization against SARS-CoV-2 Omicron variants

Graphical abstract

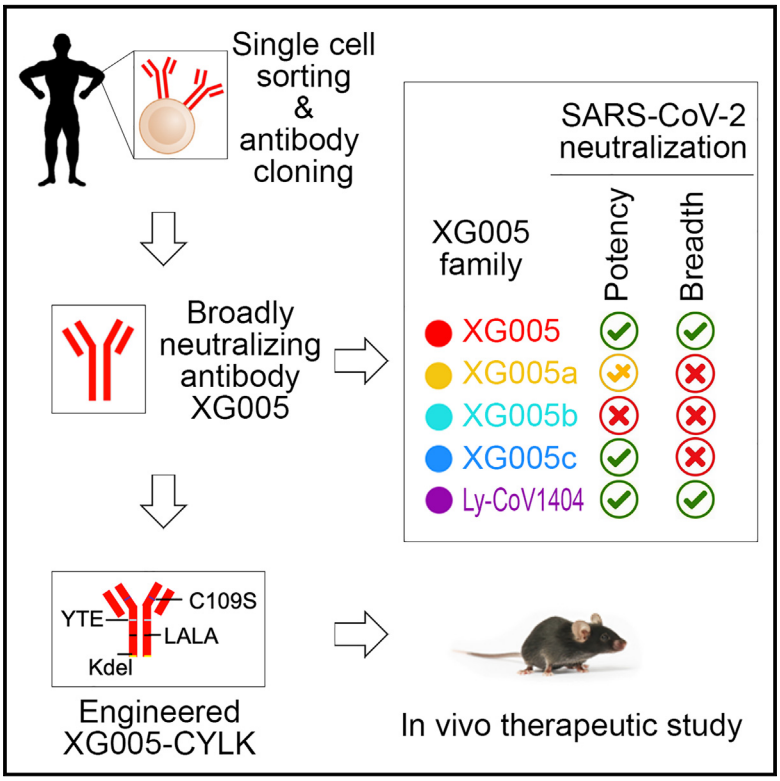

Highlights

- XG005 antibody is a potent and broad neutralizer against SARS-CoV-2 variants
- XG005 family members exhibit reduced neutralization potency and breadth
- Structure analysis and comparison identify the key amino acid residues of XG005
- Optimized XG005 exhibits a high therapeutic efficacy *in vivo*

Authors

Jianbo Wu, Zhenguo Chen, Yidan Gao, ..., Lunan Zhang, Lei Sun, Qiao Wang

Correspondence

lunan@advaccine.com (L.Z.), llsun@fudan.edu.cn (L.S.), wangqiao@fudan.edu.cn (Q.W.)

In brief

Wu et al. identify that XG005, but not its family members, is a potent and broad SARS-CoV-2 neutralizer and exhibits a high therapeutic efficacy. Structural analysis identifies the key residues of XG005. This provides a natural example to show the importance of somatic hypermutation for SARS-CoV-2 neutralization breadth and potency.

Wu et al., 2023, Cell Reports *42*, 112503
May 30, 2023
https://doi.org/10.1016/j.celrep.2023.112503

CellPress

Cell Reports

CellPress
OPEN ACCESS

Article

Fortuitous somatic mutations during antibody evolution endow broad neutralization against SARS-CoV-2 Omicron variants

Jianbo Wu,[1,6] Zhenguo Chen,[1,6] Yidan Gao,[1,6] Zegen Wang,[2,6] Jiarong Wang,[2,6] Bing-Yu Chiang,[2,6] Yunjiao Zhou,[3,6] Yuru Han,[1,6] Wuqiang Zhan,[1,6] Minxiang Xie,[1,6] Weiyu Jiang,[1] Xiang Zhang,[1] Aihua Hao,[1] Anqi Xia,[1] Jiaying He,[1] Song Xue,[1] Christian T. Mayer,[4] Fan Wu,[1,5] Bin Wang,[1,2,5] Lunan Zhang,[1,2,*] Lei Sun,[1,*] and Qiao Wang[1,7,*]

[1]Key Laboratory of Medical Molecular Virology (MOE/NHC/CAMS), Shanghai Institute of Infectious Disease and Biosecurity, Shanghai Frontiers Science Center of Pathogenic Microbes and Infection, Shanghai Fifth People's Hospital, Shanghai Key Laboratory of Medical Epigenetics, Institutes of Biomedical Sciences, School of Public Health, School of Basic Medical Sciences, Fudan University, Shanghai 200032, China

[2]Advaccine Biopharmaceuticals Suzhou Co., Ltd., Suzhou, China

[3]Fundamental Research Center, Shanghai Yangzhi Rehabilitation Hospital (Shanghai Sunshine Rehabilitation Center), School of Medicine, Tongji University, Shanghai 201619, China

[4]Experimental Immunology Branch, Center for Cancer Research, National Cancer Institute, National Institutes of Health, Bethesda, MD 20892, USA

[5]Senior author

[6]These authors contributed equally

[7]Lead contact

*Correspondence: lunan@advaccine.com (L.Z.), llsun@fudan.edu.cn (L.S.), wangqiao@fudan.edu.cn (Q.W.)

https://doi.org/10.1016/j.celrep.2023.112503

SUMMARY

Striking antibody evasion by emerging circulating severe acute respiratory syndrome coronavirus 2 (SARS-CoV-2) variants drives the identification of broadly neutralizing antibodies (bNAbs). However, how a bNAb acquires increased neutralization breadth during antibody evolution is still elusive. Here, we identify a clonally related antibody family from a convalescent individual. One of the members, XG005, exhibits potent and broad neutralizing activities against SARS-CoV-2 variants, while the other members show significant reductions in neutralization breadth and potency, especially against the Omicron sublineages. Structural analysis visualizing the XG005-Omicron spike binding interface reveals how crucial somatic mutations endow XG005 with greater neutralization potency and breadth. A single administration of XG005 with extended half-life, reduced antibody-dependent enhancement (ADE) effect, and increased antibody product quality exhibits a high therapeutic efficacy in BA.2- and BA.5-challenged mice. Our results provide a natural example to show the importance of somatic hypermutation during antibody evolution for SARS-CoV-2 neutralization breadth and potency.

INTRODUCTION

Variant strains of severe acute respiratory syndrome coronavirus 2 (SARS-CoV-2) continue to emerge and spread globally. So far, five variants of concern (VOCs) have been defined, including Alpha (B.1.1.7), Beta (B.1.351), Gamma (P.1), Delta (B.1.617.2), and the newly identified Omicron (B.1.1.529) variants.[1–3] These VOCs bear mutations in the viral spike protein (S protein), not only increasing the viral transmissibility or virulence but also facilitating the immune escape.[4–8] Many monoclonal antibodies (mAbs) identified from convalescent or vaccinated individuals showed diminished or abrogated neutralizing activity against distinct VOCs.[9,10] Especially, the newly emerged Omicron variant encodes 37 amino acid substitutions in the viral S protein, 15 of which are located in the receptor-binding domain (RBD), and causes significant humoral immune evasion, posing a remarkable challenge for the effectiveness of vaccines and mAb therapies.[11–18]

These newly emerging SARS-CoV-2 variants with strong immune escape capacity motivate researchers to identify broadly neutralizing antibodies (bNAbs) that could be of potential clinical benefit. Combining two mAbs recognizing two distinct epitopes is a popular strategy to increase the neutralizing breadth and avoid viral evasion.[19–21] For example, Eli Lilly's combination of two RBD-binding mAbs, bamlanivimab (LY-CoV555) and etesevimab, has been authorized for emergency use after exposure to the SARS-CoV-2 virus.[22] Tixagevimab (AZD8895) and cilgavimab (AZD1061) combination showed both prophylactic and therapeutic efficacy in a nonhuman primate model of SARS-CoV-2 infection.[23] A bispecific antibody through connecting two single-domain antibodies, n3113v and n3130v, also displayed exceptional neutralizing breadth and potency via inhalation administration.[21]

Meanwhile, using just a single monoclonal bNAb with high neutralization potency and breadth could also be effective for

clinical prevention or therapy. For example, LY-CoV1404 (also known as bebtelovimab) exhibits exceptional neutralizing activity against various SARS-CoV-2 variants, unaffected by most of these variant mutations.[13,18,24] However, the number of super-antibodies with extreme broad-spectrum activity and ultra-potency is still very limited, and more importantly, its evolution process *in vivo* is still largely unknown.

Here, we screen mAbs isolated from a convalescent donor with elite serum neutralizing activity[25] and identified XG005, a fully human IgG1 mAb targeting SARS-CoV-2 RBD, as an extremely potent neutralizing antibody, both *in vitro* and *in vivo*, against all currently known VOCs and the most recently emerged Omicron variants, BA.1, BA.2, BA.2.12.1, BA.3, and BA.4/5, which have severe immune escape capacity.[11,12,18,26] Structural analysis revealed that XG005 bound to an epitope that overlapped with VOC escape mutations but delicately avoided immune escape and retained its binding affinity. Moreover, three clonally related family members of XG005 isolated from the expanded B cell clone of the same donor showed reduced levels of neutralizing potency and breadth, suggesting that the resistance of XG005 evolved stochastically. Comparison of their sequences identified the somatic mutations at the amino acid residues crucial for antibody neutralizing potency and breadth. Considering that this convalescent individual donated the blood at a time when there were no emerging variants of SARS-CoV-2, we conclude that a highly potent and broad neutralizing antibody could evolve stochastically even in convalescent individuals whose sera barely neutralize SARS-CoV-2 Omicron variants.

RESULTS

Screening of antibodies isolated from a convalescent donor

We isolated mAbs, XG001–XG048, from a convalescent individual who donated blood in April 2020 when no SARS-CoV-2 variant had been reported.[25] Half of these antibodies (23/45; red name in Figure 1A) recognized the RBD of SARS-CoV-2 S protein, one-fourth (11/45; blue name in Figure 1A) were N-terminal domain (NTD)-binding antibodies, and several (5/45; green name in Figure 1A) bound the S2 stalk region.[25] To explore the cross-reactivity of these antibodies against different VOCs, we first performed an ELISA analysis against the S protein of SARS-CoV-2 and its related VOCs (Figure 1A). Among 45 antibodies, 2, 8, 5, 7 and 23 antibodies exhibited at least 25% reduction of binding activity against S protein of B.1.1.7 (Alpha), B.1.351 (Beta), P.1 (Gamma), B.1.617.2 (Delta), and B.1.1.529 (Omicron) variants, respectively (Figures 1B and S1). Some antibodies, such as XG027 and XG043, showed a substantial loss in antigen binding against most VOCs; for some others, such as RBD-binding antibody XG005 and NTD-binding antibody XG035, no loss of binding capacity was observed. Together, these results suggest that Omicron exhibited a higher level of resistance to the tested mAbs isolated from a convalescent individual and that many mAbs maintain their binding capacity against VOCs.

Neutralizing activity *in vitro* against VOCs

Antibody binding cannot predict viral neutralization. To assess the neutralization profile of these mAbs, we constructed various luciferase-expressing SARS-CoV-2 pseudoviruses, including SARS-CoV-2 Wuhan-Hu-1 (wild-type), B.1.1.7 (Alpha), B.1.351 (Beta), P.1 (Gamma), B.1.617.2 (Delta) and B.1.1.529 (Omicron) variants, and performed *in vitro* neutralization assays and calculated the IC_{50} values[25,27] (Figures 2A, 2B, and S2). Twenty-three antibodies were neutralizers against wild-type SARS-CoV-2, and all of them, except XG005, partially or entirely lost their neutralizing activity to at least one VOC (Figures 2A and 2B). Some mAbs, such as XG001 and XG002, were not neutralizing at all, while potent neutralizers XG014 and XG016 showed significant antibody evasion by only the Omicron variant (Figure 2C). XG005 exhibited ultra-potent neutralizing activities against all VOCs (Figure 2C).

Consistent with other reports that the Omicron variant escapes antibody neutralization strikingly,[12,18] nearly 90% of the our neutralizing antibodies (20/23) had impaired Omicron neutralization with a more than 3-fold increase in the antibody IC_{50} values (Figure 2B). Among the 10 Omicron-neutralizing antibodies, 9 had IC_{50} values ranging from 1 to 10 μg/mL, and only one, XG005, exhibited an impressive neutralizing potency, with an IC_{50} value of 0.005 μg/mL (Figure 2A). Taken together, these results suggest that all tested mAbs isolated from this donor, except XG005, significantly lost their neutralizing activities against VOCs, especially against Omicron variants.

Broad neutralizing activity of XG005

The outstanding neutralizing activity of XG005 led us to further assess the neutralization profile of XG005. We constructed several more types of pseudoviruses, including SARS-CoV-1, SARS-CoV-2 variants (B.1.351-L242H, B.1.617.1 [Kappa], C.37 [Lambda], B.1.621 [Mu]), and SARS-CoV-2 Omicron variants (BA.1, BA.2, BA.2.12.1, BA.3, BA.4/5) and performed pseudovirus neutralization assays. XG005 remained potent in neutralizing all these variants, including Omicron sublineages, with IC_{50} values of 0.008 μg/mL or lower but had no neutralization activity against SARS-CoV-1 (Figures 2D and 2E). Together, the potent and broad neutralizing activity of XG005 indicates that there is still a highly conserved RBD epitope for antibody binding that is not affected by any escape mutations in SARS-CoV-2 variants.

Structural and functional basis of XG005 neutralization and retained potency

To understand the structural basis for the neutralizing activity of XG005, we determined the cryoelectron microscopy (cryo-EM) structure of the SARS-CoV-2 wild-type S trimer complexed with XG005 Fab, revealing a conformation of two "up" and one "down" RBD with three Fabs (UDU with three Fabs, PDB: 7V26, 3.8 Å resolution).[27] To further understand its broad neutralizing activity, we determined the cryo-EM structure of the SARS-CoV-2 Omicron S trimer complexed with XG005 (OS-XG005) (Figures S3 and S4; Table S1). Other than the UDU conformation with three Fabs (PDB: 7YCZ, 3.24 Å), the OS-XG005 exhibited another two states, one "up" and two "down" RBDs with two Fabs (UDD with two Fabs, PDB: 7YD0, 3.62 Å) and one "up" and two "down" RBDs with three Fabs (UDD with three Fabs, PDB: 7YCY, 3.74 Å) (Figure 3A). Among these conformations, the "up" RBDs opened almost in the same orientation, while the orientations of "down" RBDs were different, which might result from the conformations of the other two RBDs (Figure 3B).

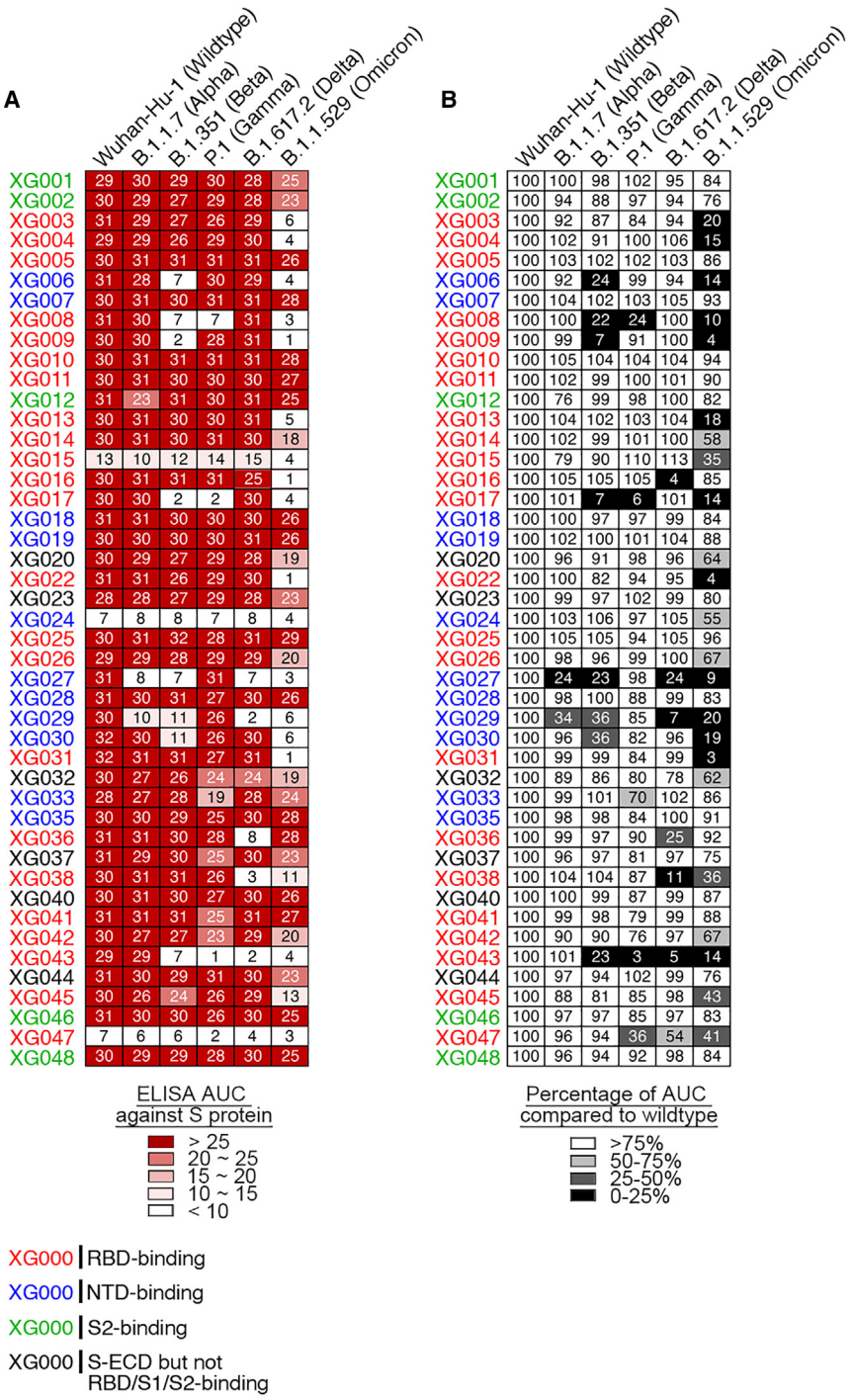

Figure 1. ELISA cross-reactivity of anti-S monoclonal antibodies (mAbs)

(A) Graphs show antibody ELISA reactivity against S proteins of wild-type SARS-CoV-2 and its five related VOCs. The six tested ELISA antigens include S proteins of Wuhan-Hu-1 (wild-type), B.1.1.7 (Alpha), B.1.351 (Beta), P.1 (Gamma), B.1.617.2 (Delta), and B.1.1.529 (Omicron). ELISA area under the curve (AUC) values were calculated for all 45 mAbs isolated from a convalescent donor with a potent serum neutralizing activity.[25] Representative of two experiments. The names of mAbs are color coded: red, RBD-binding mAb; blue, NTD-binding mAb; green, S2-binding mAb; and black, S-ECD- but not RBD/S1/S2-binding mAb.

(B) Percentage change in ELISA AUC relative to wild-type S protein. ELISA AUC results are presented as percentage of AUC normalized to the reactivity against Wuhan-Hu-1 (wild-type) S protein and are illustrated by colors: black, 0%–25%; dark gray, 25%–50%; light gray, 50%–75%; and white, >75%.

See also Figure S1.

Comparison of the interface regions of wild-type RBD-XG005[27] and Omicron RBD-XG005 showed that the XG005 interacted with wild-type and Omicron RBDs in a very similar way. The tight contacts between XG005 and Omicron RBDs mainly resulted from extensive hydrophilic interactions. Three mutation residues (N440K, G446S, and N501Y) of the Omicron S were located in the XG005-recognizing epitope (Figures 4A and 4B). Specifically, although N501Y mutation led to the loss of two hydrogen bonds between N501 of the wild-type RBD and N33 of XG005 light-chain complementarity determining region 1 (CDRL1) (Figures 4C and 4D), G446S mutation introduced two hydrogen bonds between Omicron-S S446 and T96 of XG005 CDRL3 (Figures 4C and 4D). Moreover, N440K mutation destroyed the hydrogen bonds between residues N440/L441 of the wild-type RBD and Y34/G33 of XG005 CDRL1/heavy-chain CDR2 (CDRH2) but rescued one hydrogen bond between K440 of the Omicron RBD and A103 of XG005 CDRH3 (Figures 4C and 4D). In addition, one hydrogen bond formed between N450 of the Omicron RBD and D58 of XG005 CDRH2 as a compensation (Figures 4C and 4D). Therefore, the three Omicron mutations (N440K, G446S, and N501Y) did not disrupt the RBD-XG005 interaction (Figure 4E).

Based on the cryo-EM structure, the residues N450, V445, G447, N439, and Q506 of SARS-CoV-2 S protein were crucial for XG005 recognition, while SARS-CoV-2 VOCs bear no amino acid change on these residues. This is consistent with the overall high neutralizing potency of XG005 against all tested variants.

Clonally related neutralizing antibodies of XG005

It has been shown recently that a higher level of somatic hypermutation acquired in the months post-infection or by a vaccine booster shot provides some antibodies with greater neutralizing

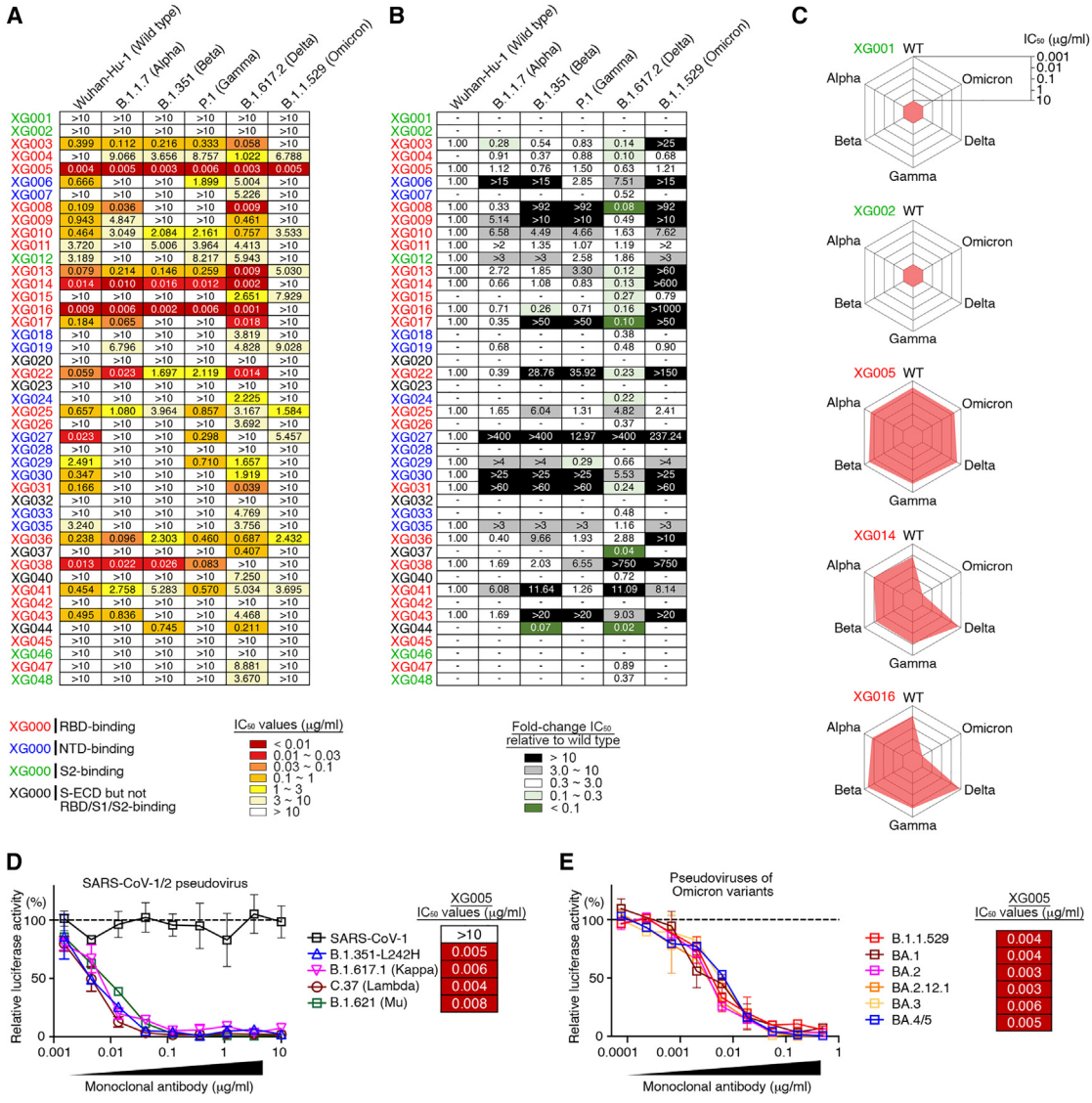

Figure 2. Cross-neutralizing activity

(A) Pseudovirus neutralization assays by mAbs. IC_{50} values for all 45 antibodies measured against Wuhan-Hu-1 (wild-type), B.1.1.7 (Alpha), B.1.351 (Beta), P.1 (Gamma), B.1.617.2 (Delta), and B.1.1.529 (Omicron) pseudoviruses. Antibodies with IC_{50} values above 10 μg/mL were shown as >10 μg/mL. Mean of two independent experiments. The names of mAbs are color coded: red, RBD-binding mAb; blue, NTD-binding mAb; green, S2-binding mAb; and black, S-ECD- but not RBD/S1/S2-binding mAb.

(B) Fold change in IC_{50} values relative to Wuhan-Hu-1 (wild-type) SARS-CoV-2. Reduced neutralizing activities (increased IC_{50} values) are presented in black (>10-fold) or gray (3- to 10-fold), while enhanced neutralization (decreased IC_{50} values) are shown in dark green (<10%) and light green (10%–30%).

(C) Spider charts for IC_{50} values of representative mAbs.

(D and E) Neutralization potency of XG005. Luciferase-based pseudoviruses of SARS-CoV-1, four SARS-CoV-2 variants (D) and six Omicron variants (E) were used for cell infection, and the luciferase signal after infection was determined as a surrogate of infection and normalized to the no antibody control (dashed line). *In vitro* neutralization assays for each antibody were performed at least two times, presented as mean ± SEM. IC_{50} values, mean of two independent experiments. See also Figure S2.

potency and breadth, suggesting that increased antibody diversity may improve antibody resistance to viral escape mutations.[28–30] However, XG005 was cloned from a donor early in convalescence, and its somatic mutation level is low, with only 6 amino acid substitutions in both heavy- and light-chain V regions compared with germline sequences (Figure 5A). To understand the evolution process of XG005 for Omicron neutralization, we isolated three clonally related antibodies of XG005 from the same donor[25] and named them XG005a, XG005b, and XG005c.

XG005 and its three family members were all encoded by IGHV2-5/IGLV2-14 (Figure S5A). Sequence alignment between their heavy and light chains suggested a high similarity, including

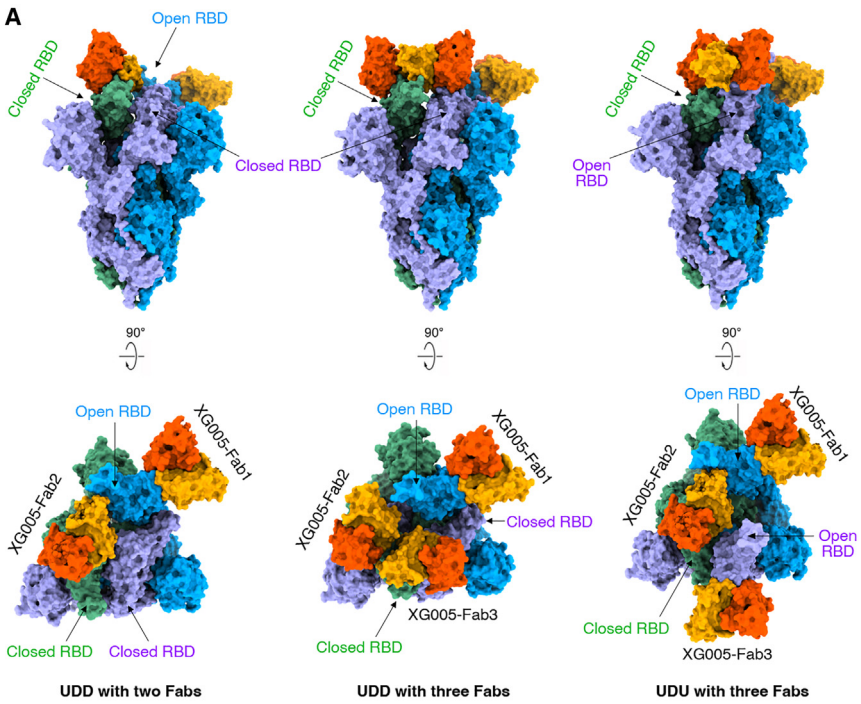

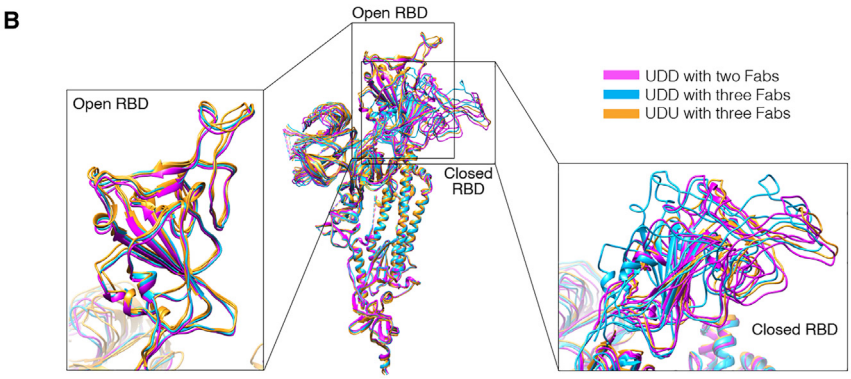

Figure 3. Cryo-EM structures of XG005 complexed with Omicron S trimer

(A) XG005 binds to Omicron S trimer in three states: one "up" RBD and two "down" with two Fabs (UDD with two Fabs), one "up" RBD and two "down" with three Fabs (UDD with three Fabs), and two "up" RBDs and one "down" RBD with three Fabs (UDU with three Fabs). Two perpendicular views of Omicron S-XG005 depict the surface. The XG005 VH/CH and VL/CL domains are colored in orange and yellow, respectively. Three S protomers of Omicron S trimer are colored in blue, green, and purple, respectively.

(B) Comparison of all S monomers of the three states in ribbon, showing that all "up" RBDs are at the similar orientation while the down RBDs adopt different orientations. The monomers of three states are colored in magenta, blue, and yellow, respectively, VH: variable region of heavy chain; CH: constant region of heavy chain, VL: variable region of light chain; CL: constant region of light chain.

See also Figures S3 and S4 and Table S1.

their CDR3 sequences of both heavy and light chains (Figure 5A). The levels of somatic hypermutation for all XG005 family members were low, and XG005a–XG005c had even lower levels of somatic hypermutations compared with XG005 (Figure 5A).

We further evaluated their neutralization potency against a panel of pseudotyped viruses of SARS-CoV-2 variants. XG005 and its three family antibodies exhibited striking disparity in neutralizing activity and breadth (Figures 5B and S5B). Specifically, XG005b displayed minimal activity against most SARS-CoV-2 variant pseudoviruses, with IC_{50} values ranging from 1.517 to >10 μg/mL (Figures 5B and 5C). XG005a neutralized most variants, with IC_{50} values ranging from 0.023 to 0.267 μg/mL for all variants except Omicron, for which the IC_{50} was >10 μg/mL (Figures 5B and 5C). XG005c potently neutralized the majority of SARS-CoV-2 variant pseudoviruses (IC_{50} values of 0.001–0.058 μg/mL) but exhibited a partial loss of potency against Omicron (IC_{50} value of 1.995 μg/mL) (Figures 5B and 5C).

To specifically examine the potential influence of somatic hypermutation in the CDRH3 sequence, we generated a series of XG005 mutants with only one amino acid substituted in its CDRH3 region (Figure 5D) and assessed their neutralization profile (Figure 5E). Substitution of XG005 CDR3 amino acids with the corresponding residues of its family members (T101A and A103T but not A102S) showed reduced neutralization against Omicron (Figure 5E). All alanine substitutions, except D108A, within the XG005 CDRH3 sequence affected the neutralization potency and breadth (Figures 5D and 5E). Together, the special CDRH3 sequence of XG005 confers its broad neutralization.

Ly-CoV1404 and XG005

XG005 was encoded by IGHV2-5/IGLV2-14. Similar to XG005, a well-known broad and potent neutralizing mAb, LY-CoV1404 (bebtelovimab), was also encoded by IGHV2-5/IGLV2-14[24,31] (Figure 5A).

By using our *in vitro* pseudotyped virus-based neutralization assay, we assessed the neutralization profile of Ly-CoV1404 and showed that Ly-CoV1404 and XG005 showed comparable neutralization titers against SARS-CoV-2 and its variants (Figures 5B and 5C).

Comparison of the cryo-EM structures of both XG005 and LY-CoV1404 revealed very high levels of similarity, including the RBD interfaces and the key amino acid residues for RBD interaction (Figure S6). These results suggest that the cryo-EM structure of XG005 is extraordinarily comparable with that of LY-CoV1404.

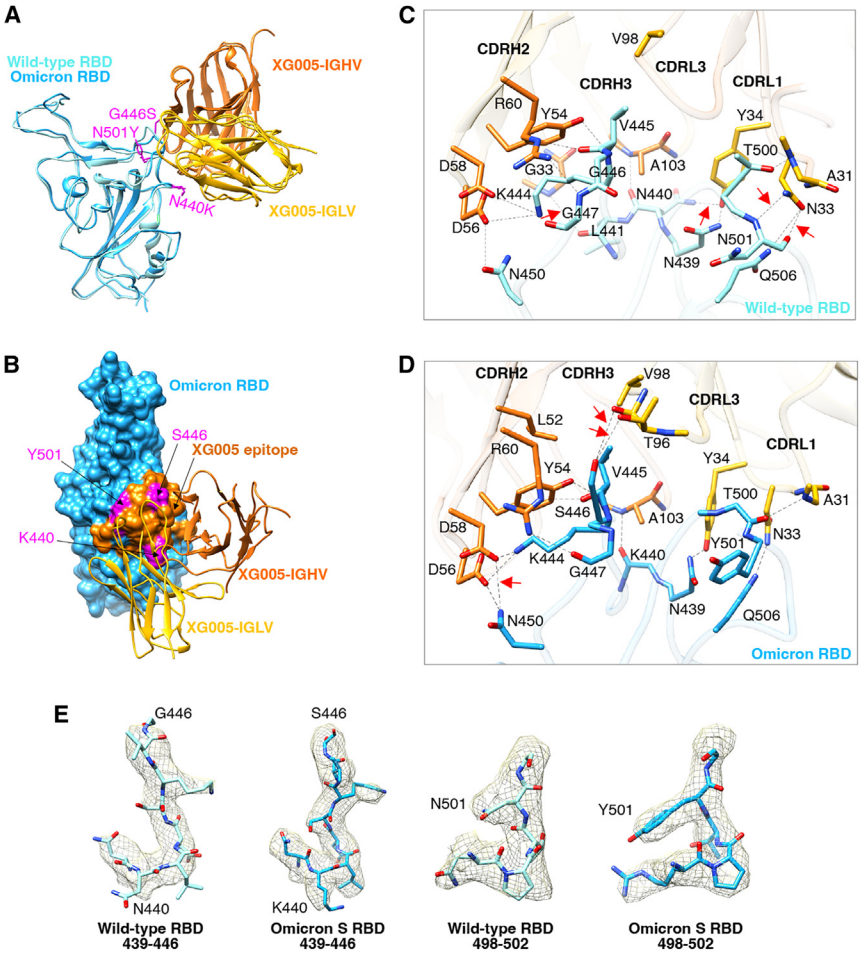

Figure 4. Comparison the interface between SARS-CoV-2 wild-type RBD-XG005 and Omicron RBD-XG005

(A) Comparison the models of SARS-CoV-2 wild-type RBD-XG005 and Omicron RBD-XG005. Wild-type RBD and Omicron RBD were shown as ribbons and colored in light sky blue and deep sky blue, respectively. The XG005 IGHV and IGLV are colored in orange and yellow, respectively. Omicron mutation residues located in the XG005 epitope are shown as atoms and colored in magenta.

(B) The model of Omicron RBD-XG005. Omicron RBD is displayed in deep sky blue. The XG005 epitope is colored in orange, and Omicron mutation residues within the interface located in XG005 epitope are shown as atoms and colored in magenta.

(C and D) The detailed interfaces between SARS-CoV-2 wild-type RBD and XG005 (C) and between Omicron RBD and XG005 (D). The red arrows emphasize the specific interactions between RBD and XG005.

(E) Density maps of residues around the wild-type RBD-XG005 interface or Omicron RBD-XG005 interface. Density maps were generated by DeepEMhancer. The Omicron mutations located in the XG005 epitope are labeled.

Therefore, a slight alteration of amino acid residues, for example between XG005 and XG005b, might largely reduce the neutralization potency and breadth, while on the other hand, interestingly, mAbs identified from different donors with more distinct CDRH3 sequences (Figures 5A and 5D), such as XG005 and Ly-CoV1404, showed a similar level of neutralization potency and breadth.

Structural comparison for the key amino acid residues during antibody evolution

XG005 exhibited ultra-potent neutralizing activity against the B.1.1.529 (Omicron) pseudovirus, while none of the XG005 family members showed comparable activity. We further measured their ELISA binding activity against the S protein of B.1.1.529 (Omicron). As expected, similar binding activities were observed between XG005 and XG005c (ELISA area under the curve [AUC] ~30). XG005a had slightly reduced binding activity (ELISA AUC ~26), while XG005b binding capacity was abolished by Omicron mutations (ELISA AUC ~9) (Figure S5C).

To reveal the underlying molecular mechanism, we performed structural analysis and modeled the interactions between the Omicron RBD and three XG005 family members (Figure 6A). The structural models of XG005a, XG005b, and XG005c were generated based on the XG005 structure by SWISS-MODEL.[32] The structures of all four XG005 family members were similar, with 15 amino acid residues in IGHV and 14 amino acid residues in IGLV involved in the recognition of the Omicron RBD (Figure 5A). Superimposed structural models showed that 8 of 11 key residues involved in the interaction were conserved among XG005 family members, including Y54, L52, R60, D56, and D58 in IGHV and Y34, N33, and V98 in IGLV. However, although the residue D58 in IGHV was conserved among XG005 family members, this residue in XG005a, XG005b, and XG005c shifted away and damaged the hydrogen bond between N450 of the Omicron RBD and D58 of antibody heavy chain, thus causing the reduced binding affinity against the Omicron RBD (Figure 6B).

The other three key residues for Omicron RBD recognition were A103 in the heavy chain and T96/A31 in the Lambda light chain of XG005 (Figures 6A and 6B). Both A103 in XG005 and T103 in other family members bound the SARS-CoV-2 RBD with no difference. For residue 96 of IGLV, the S96T mutation in XG005, XG005a, and XG005c established a hydrogen bond between S446 of the Omicron RBD and T96 of IGLV, while the lack of this somatic mutation in XG005b failed to do so (Figure 6B). In addition, the G31A mutation in XG005/XG005c IGLV was a key mutation for recognizing the Omicron RBD. However, for XG005a, a G31D mutation at this residue introduced a clash between the Omicron RBD and D31 of XG005a, reducing XG005a's binding affinity with the Omicron RBD (Figure 6B). Together, these results provided a structural explanation that

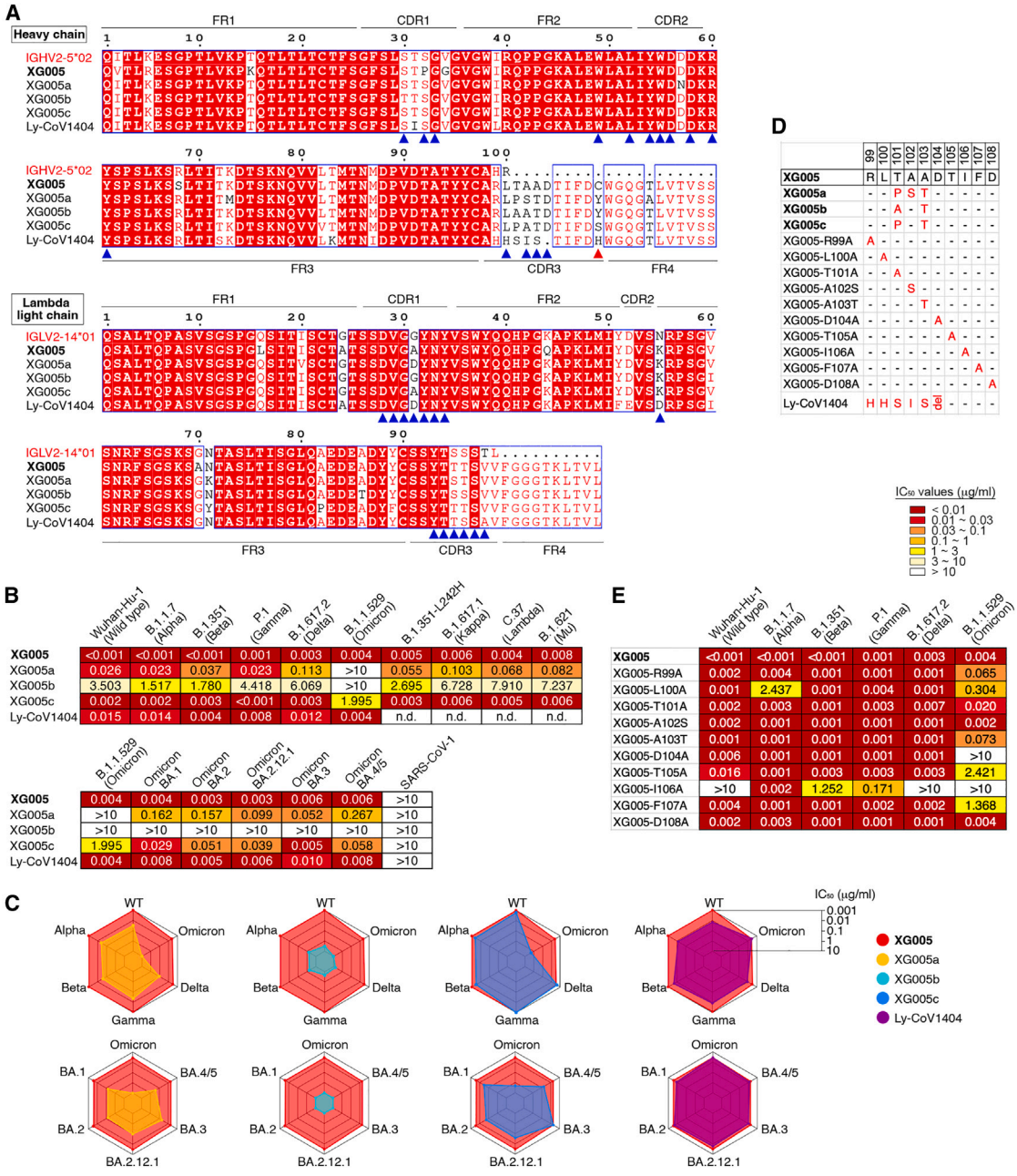

Figure 5. Clonally related family members of XG005 exhibited striking disparity in neutralizing activity and breadth

(A) Amino acid sequence alignment for XG005 and its clonally related family members (XG005a, XG005b, and XG005c) and Ly-CoV1404.[24,31] IGHV2-5*02 and IGLV2-14*01 are the germline reference sequences assigned by IMGT/V-QUEST for IGHV and IGLV, respectively. Boxed red areas are shared among antibodies. The 15 amino acid residues in XG005 IGHV and 14 amino acid residues in XG005 IGLV involved in the recognition of the Omicron RBD are marked by blue arrowheads. The red arrowhead indicates the noncanonical cysteine C109 located in the CDR3 region of XG005 heavy chain.

(B) Pseudovirus neutralization assays. IC_{50} values for mAbs measured against pseudoviruses of SARS-CoV-1 and SARS-CoV-2 and its variants. Antibodies with IC_{50} values above 10 μg/mL were shown as >10 μg/mL. The abbreviation n.d. indicates "not determined." Mean of two independent experiments.

(C) Spider charts for IC_{50} values of XG005, its three family members, and Ly-CoV1404, which was also encoded by IGHV2-5/IGLV2-14 as XG005.

(D) CDRH3 amino acid sequences of a series of XG005 mutants. The XG005 CDRH3 amino acid sequence is shown completely, while for other mAbs, only the different amino acid residues are labeled in red. The abbreviation del means "amino acid deletion," while the "-" represents the same amino acid with XG005 CDRH3.

(E) Pseudovirus neutralization assays using XG005 mutants. IC_{50} values for a series of XG005 mutants against pseudoviruses of SARS-CoV-2 and its variants. Mean of two independent experiments.

See also Figures S5 and S6.

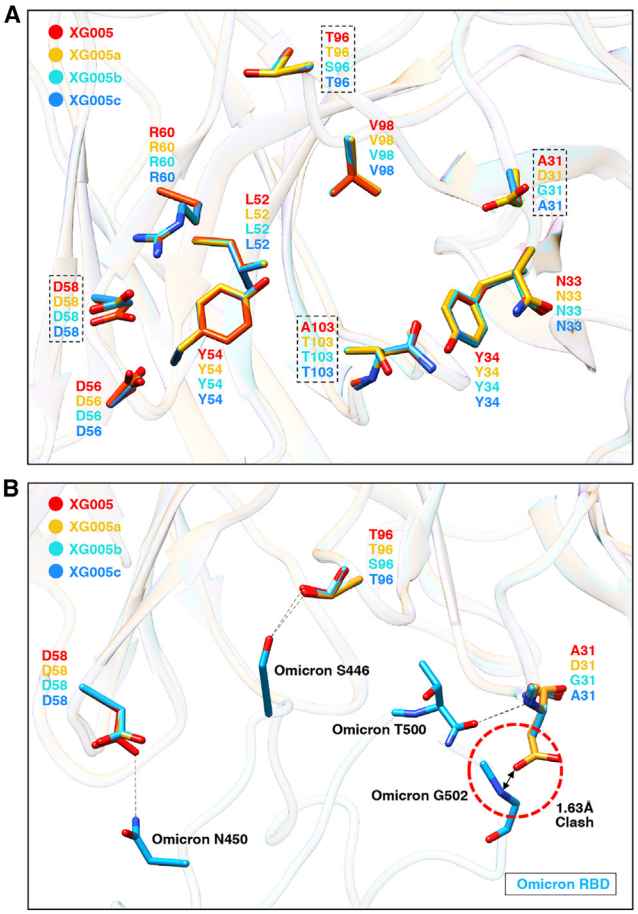

Figure 6. Structural comparison of XG005 family members revealed the key somatic mutations for broad and potent neutralization

(A) Structural comparison of XG005 (red ribbon), XG005a (yellow ribbon), XG005b (cyan ribbon), and XG005c (blue ribbon). The structural models of XG005a, XG005b, and XG005c were generated by SWISS-MODEL. The residues involved in RBD binding are shown in sticks. The residues that might disturb the interactions between the RBD and Fabs are emphasized by dashed squares.

(B) The interfaces between Omicron RBD (deep sky blue ribbon) and XG005/XG005a/XG005b/XG005c. The distinct key residues among XG005, XG005a, XG005b, and XG005c were labeled. Hydrogen bonds are shown as black dashed lines. Red dashed circle highlights the clash between the Omicron RBD and D31 of XG005a.

XG005 neutralized more potently than XG005c and that XG005c neutralized better than XG005a and XG005b (Figures 5B and 5C).

Engineered XG005 with reduced enhancement and extended half-life

Our previous data showed that XG005 induced antibody-mediated viral entry and S protein-mediated membrane fusion through its interaction with Fc receptor (FcR), implying the potential side effect for antibody prophylaxis and therapy.[25,27] As expected, LY-CoV1404 also induced *in vitro* antibody-dependent enhancement (ADE) of viral entry (Figure 7A). To eliminate its ADE of viral entry, we thus engineered XG005 Fc amino acids to reduce its FcR interactions (GRLR, G239R/L331R, or LALA, L237A/L238A, modifications). *In vitro* SARS-CoV-2 pseudovirus (ADE) assays[25] showed that the engineered Fc variants of XG005 with GRLR or LALA substitutions induced no ADE effect in cultured Raji cells, while a strong *in vitro* ADE effect was observed in Raji cells treated with wild-type XG005 (Figure 7B).

XG005 had a noncanonical cysteine (C109; red arrowhead in Figure 5A) in the CDR3 region of the XG005 heavy chain. To avoid the potential aggregation and antibody instability triggered by this noncanonical cysteine through intramolecular scrambling or intermolecular disulfide formation,[33] we substituted the cysteine at position 109 with tyrosine (Y) or serine (S) residues, the corresponding amino acid residues in XG005b and XG005c, respectively (Figure 5A). Both substitutions (XG005-C109Y and XG005-C109S) showed no reduction in neutralizing activity against SARS-CoV-2 variants (Figure S7).

We further engineered XG005 Fc domain to extend the antibody half-life (YTE, M255Y/S257T/T259E, or LS, M431L/N437S) and to reduce antibody heterogeneity (Kdel, deletion of the C-terminal lysine in immunoglobulin [Ig] heavy chain). Pharmacokinetic analyses in a humanized FcRn transgenic mouse showed that XG005 had a longer half-life than LY-CoV1404 and that the YTE substitution in XG005 significantly extended its serum half-life (Figure 7C). Moreover, we performed *in vitro* neutralization assays to ensure that none of these Fc substitutions affected the *in vitro* neutralizing activity of XG005 (Figure S8).

Together, to facilitate and improve therapeutic use, we engineered XG005, reduced its ADE effect, increased its half-life, optimized the antibody production and quality, and finally developed XG005-C109S-YTE-LALA-Kdel (XG005-CYLK) for the following therapeutic evaluation *in vivo*.

Therapeutic activity of XG005-CYLK

We first confirmed the neutralizing activity of XG005-CYLK using authentic SARS-CoV-2 viruses BA.2 and BA.5 (Figure 7D). As shown, significant inhibitory activities against BA.2 and BA.5 infection were observed for XG005-CYLK, with IC_{50} values of 0.033 and 0.023 μg/mL, respectively.

We next sought to evaluate the therapeutic activity of XG005-CYLK in an established human ACE2 transgenic mouse model. Mice were intranasally challenged with BA.2 or BA.5 virus using 1×10^5 focus-forming units (FFUs) and, 4 h post-infection, were intraperitoneally treated with a single dose of antibody XG005-CYLK or the same volume of PBS as control (Figure 7E). Two days post-inoculation, the viral loads in the lungs reached $3.7–6.1 \times 10^5$ FFUs for BA.2 and $1.03–1.37 \times 10^6$ FFUs for BA.5 in the control groups of mice treated with PBS (Figures 7F and 7G). Compared with the control groups, a single dose of XG005-CYLK (2.5, 7, or 21 mg/kg for BA.2; 1, 5, or 10 mg/kg for BA.5) efficiently reduced the viral loads by more than 1,000-fold in the lungs (Figures 7F and 7G). However, decreased levels of XG005-CYLK (0.2 and 0.04 mg/kg for BA.5) were not sufficient to suppress the lung viral loads (Figure 7G).

Collectively, these results suggest that rare B cells elicited by just wild-type SARS-CoV-2 infection retained broad neutralization against the currently circulating SARS-CoV-2 variants, and

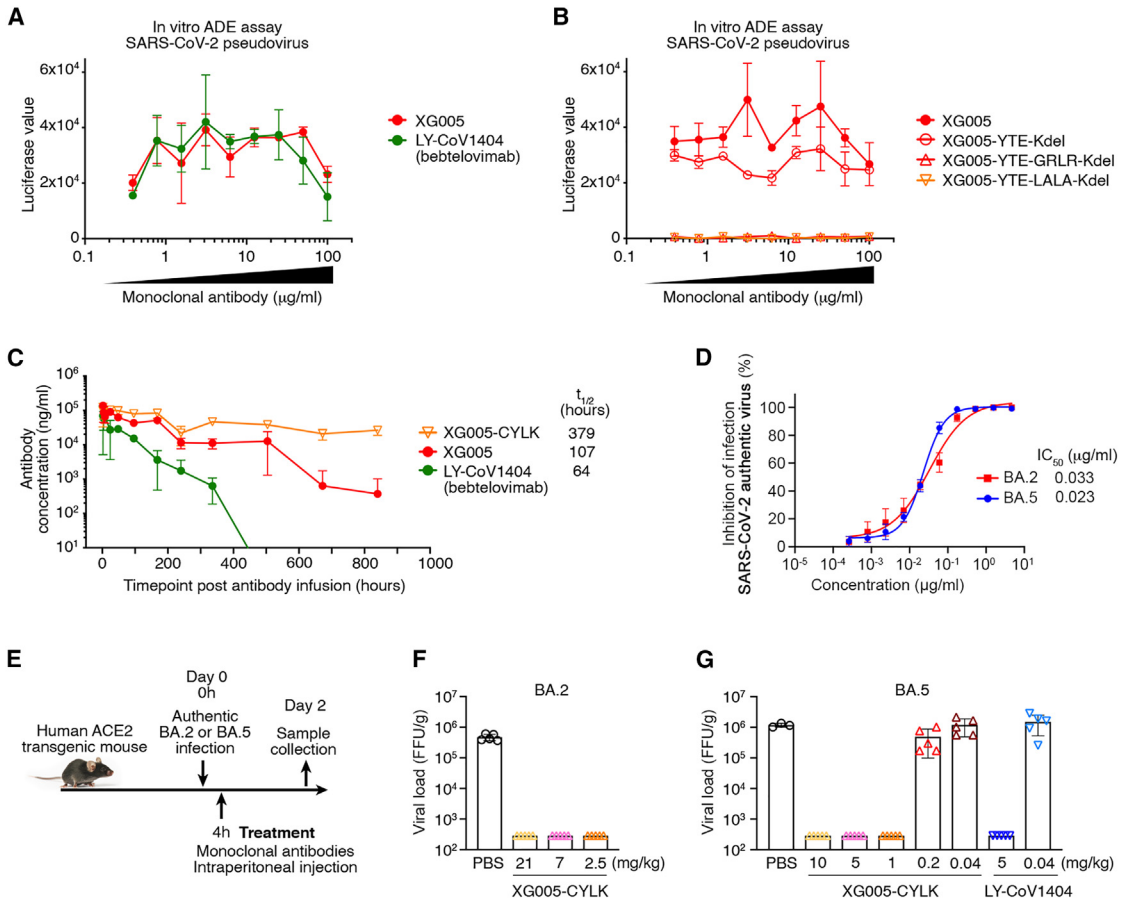

Figure 7. XG005-CYLK is therapeutic against BA.2 and BA.5 *in vivo*

(A) *In vitro* ADE effects induced by both XG005 and its counterpart LY-CoV1404 (bebtelovimab). *In vitro* ADE assays were performed in the Raji cells by using luciferase-expressing SARS-CoV-2 pseudovirus. The presence of various dilutions of antibodies induced distinct levels of luciferase signal, while the luciferase signal without adding any antibody was almost zero.

(B) No ADE effect induced by the GRLR and LALA versions, but not the YTE version, of the Fc-engineered XG005 antibodies.

(C) Pharmacokinetics of single-dose mAbs, XG005, XG005-C109S-YTE-LALA-Kdel (XG005-CYLK), and LY-CoV1404 in transgenic mice, C57BL/6JSmoc, which expressed human neonatal Fc receptor (hFcRn).

(D) XG005 potently neutralizes authentic SARS-CoV-2 BA.2 and BA.5 viruses. The *in vitro* neutralization assays were repeated at least twice.

(E) Diagram of antibody treatment protocols for human ACE2 transgenic mice intranasally challenged with BA.2 or BA.5 viruses.

(F–G) Virus titers in lung tissues of mice collected 2 days after BA.2 (F) or BA.5 (G) viral infection. Data are presented as mean ± SD. Each group contains three to five individual mice.

See also Figures S7 and S8.

the corresponding mAbs could be engineered as potent therapeutics.

DISCUSSION

In this article, we examined the binding capacity and neutralizing activity of 45 mAbs isolated from a convalescent individual who donated blood in April 2020. Among them, the XG005 mAb showed potent and broad neutralizing activity against all variants, including the BA.2, BA.2.12.1, and BA.4/5 subvariants. Treatment experiments in mice with engineered XG005 alone showed efficient viral-controlling effect *in vivo*. Therefore, the high threshold against virus escape provided by an antibody cocktail would also be achieved by a single mAb alone.

Cryo-EM structure explained how XG005 avoided immune escape and maintained neutralization potency. Although many bNAbs against Omicron bound to an outer surface of the RBD,[34–36] XG005 recognized the receptor-binding motif (RBM), which bound to ACE2 receptor and is highly mutated in the Omicron subvariants.[37] However, distinct from the immune escape of most RBM-targeting antibodies, XG005 delicately avoided significant loss of neutralization despite the three Omicron amino acid mutations (N440K, G446S, and N501Y) located in the XG005-recognizing epitope. Newly formed hydrogen bonds and salt bridges simultaneously rescued the loss of hydrogen bonds between XG005 and Omicron S protein (Figure 4). This effective compensation mechanism plays an important role for recognizing various SARS-CoV-2 variants.

XG005 was an IGHV2-5/IGLV2-14-encoded RBD antibody, while antibodies LY-CoV1404 (bebtelovimab),[24] 2–7,[38] and XGv265[39] were also IGHV2-5/IGLV2-14 encoded.[31] All of these mAbs retained their neutralizing activity against SARS-CoV-2 variants, especially against Omicron and its sublineages. Compared with the IGHV1-58/IGKV3-20-encoded RBD-binding public antibody clonotype, the IGHV2-5/IGLV2-14-encoded RBD antibodies with increased breadth of neutralization are perhaps the most cross-neutralizing public antibody clonotype.[31]

In our study, three other family members of XG005 (XG005a, XG005b, and XG005c) that we cloned from the same expanded B cell clone of the same donor showed significant reduction of neutralization potency and breadth. Nevertheless, sequence comparison showed only very little difference of these mAbs compared with XG005. Structural remodeling suggested the key amino acid residues on XG005 during antibody evolution for its neutralizing activity against Omicron subvariants. Considering that there was still no Omicron variant during blood donation in April 2020, these results suggest that XG005 was the rare product of random somatic hypermutation in germinal centers. Similarly, LY-CoV1404 was also cloned from a convalescent individual in early 2020.[24] Interestingly, the third dose of vaccine booster shot with wild-type SARS-CoV-2 facilitated the generation of potent bNAbs against VOCs and Omicron subvariants.[39] Together, we conclude that exposure to wild-type SARS-CoV-2 or its surface protein is sufficient to elicit bNAbs against recently emerged or even future SARS-CoV-2 variants.

Limitations of the study

In this study, we only cloned and analyzed four antibody members of XG005 family, including XG005 itself. Although Ly-CoV1404 was also included for analysis and comparison, it was cloned from a different donor with a very distinct CDRH3 sequence. Therefore, more cloned XG005 family members from the same individual would provide more details of these antibodies' evolution and reveal how occasionally a mAb with potent and broad neutralizing activity could be generated. Moreover, XG005, as its counterpart Ly-CoV1404, lost most of its neutralizing activity against the newly emerged SARS-CoV-2 variants XBB and BQ.1. Therefore, whether XG005 could be further mutated to achieve increased neutralization potency and breadth has not been studied here.

STAR★METHODS

Detailed methods are provided in the online version of this paper and include the following:

- KEY RESOURCES TABLE
- RESOURCE AVAILABILITY
  - Lead contact
  - Materials availability
  - Data and code availability
- EXPERIMENTAL MODEL AND SUBJECT DETAILS
- METHOD DETAILS
  - ELISA
  - Generation of SARS-CoV-1/2 pseudoviruses
  - *In vitro* pseudotyped virus-based neutralization assay for SARS-CoV-2
  - *In vitro* neutralization assay using authentic BA.2 and BA.5 viruses
  - Antibody cloning and production
  - Expression and purification of SARS-CoV-2 Omicron S trimer
  - Cryo-EM sample preparation
  - Cryo-EM data collection and image processing
  - Model building and refinement
  - Human ACE2 transgenic mice and *in vivo* studies
  - Pharmacokinetic analysis
- QUANTIFICATION AND STATISTICAL ANALYSIS

SUPPLEMENTAL INFORMATION

Supplemental information can be found online at https://doi.org/10.1016/j.celrep.2023.112503.

ACKNOWLEDGMENTS

We thank the Center of Cryo-Electron Microscopy at Fudan University for the support on cryo-EM data collection and Guangzhou Custom Technology Center for the support of *in vivo* challenge study in a Biosafety Level 3 (BSL-3) laboratory. We thank Bo Chen, Xulong Feng, Xinyi An, Miaomiao Wang, Yongpeng Xu, and Qingyu Yang at Advaccine Biopharmaceuticals Suzhou Co., Ltd., for the help of cell-based and pharmacokinetics assays. We also thank Dr. Xiangxi Wang at the Institute of Biophysics, Chinese Academy of Sciences for providing the S proteins of several SARS-CoV-2 variants for ELISAs. This work was supported by the National Key Research and Development Program (2021YFA1301404), the National Natural Science Foundation of China (32070947), and the Ministry of Science and Technology (China) of China (2021YFC2302500). The project was also supported by Shanghai Municipal Science and Technology Major Project (ZD2021CY001) and by the Guangzhou Laboratory (SRPG22-003). This work was supported by funding from the Intramural Research Program, National Institutes of Health, National Cancer Institute, Center for Cancer Research. The content of this publication does not necessarily reflect the views or policies of the Department of Health and Human Services nor does mention of trade names, commercial products, or organizations imply endorsement by the US government. The content is solely the responsibility of the authors and does not necessarily represent the views of any of the funding agencies or individuals.

AUTHOR CONTRIBUTIONS

Conceptualization, Q.W.; investigation, J.W., Z.C., Y.G., Z.W., J.W., B.-Y.C., Y.Z., Y.H., W.Z., M.X., W.J., X.Z., A.H., A.X., J.H., and S.X.; software, J.W., W.Z., and Z.C.; formal analysis, J.W., W.Z., Y.Z., B.W., Z.W., J.W., B.-Y.C., L.Z., L.S., and Q.W.; writing – original draft, Q.W.; writing – review & editing, J.W., W.Z., C.T.M., B.-Y.C., B.W., L.S., and Q.W.; visualization, J.W., W.Z., L.S., and Q.W.; supervision, B.W., F.W., L.Z., L.S., and Q.W.; funding acquisition, B.W., F.W., L.Z., L.S., and Q.W.

DECLARATION OF INTERESTS

A patent application encompassing aspects of this work has been filed with Q.W. and L.Z. listed as inventors.

Received: January 4, 2022
Revised: April 11, 2023
Accepted: April 26, 2023
Published: May 3, 2023

REFERENCES

1. Mannar, D., Saville, J.W., Zhu, X., Srivastava, S.S., Berezuk, A.M., Tuttle, K.S., Marquez, A.C., Sekirov, I., and Subramaniam, S. (2022). SARS-CoV-2 Omicron variant: antibody evasion and cryo-EM structure of spike protein-ACE2 complex. Science *375*, 760–764. https://doi.org/10.1126/science.abn7760.
2. Karim, S.S.A., and Karim, Q.A. (2021). Omicron SARS-CoV-2 variant: a new chapter in the COVID-19 pandemic. Lancet *398*, 2126–2128. https://doi.org/10.1016/S0140-6736(21)02758-6.
3. Viana, R., Moyo, S., Amoako, D.G., Tegally, H., Scheepers, C., Althaus, C.L., Anyaneji, U.J., Bester, P.A., Boni, M.F., Chand, M., et al. (2022). Rapid epidemic expansion of the SARS-CoV-2 Omicron variant in southern Africa. Nature *603*, 679–686. https://doi.org/10.1038/s41586-022-04411-y.
4. Planas, D., Veyer, D., Baidaliuk, A., Staropoli, I., Guivel-Benhassine, F., Rajah, M.M., Planchais, C., Porrot, F., Robillard, N., Puech, J., et al. (2021). Reduced sensitivity of SARS-CoV-2 variant Delta to antibody neutralization. Nature *596*, 276–280. https://doi.org/10.1038/s41586-021-03777-9.
5. Wang, P., Nair, M.S., Liu, L., Iketani, S., Luo, Y., Guo, Y., Wang, M., Yu, J., Zhang, B., Kwong, P.D., et al. (2021). Antibody resistance of SARS-CoV-2 variants B.1.351 and B.1.1.7. Nature *593*, 130–135. https://doi.org/10.1038/s41586-021-03398-2.
6. Mlcochova, P., Kemp, S.A., Dhar, M.S., Papa, G., Meng, B., Ferreira, I.A.T.M., Datir, R., Collier, D.A., Albecka, A., Singh, S., et al. (2021). SARS-CoV-2 B.1.617.2 Delta variant replication and immune evasion. Nature *599*, 114–119. https://doi.org/10.1038/s41586-021-03944-y.
7. Wang, G.L., Wang, Z.Y., Duan, L.J., Meng, Q.C., Jiang, M.D., Cao, J., Yao, L., Zhu, K.L., Cao, W.C., and Ma, M.J. (2021). Susceptibility of circulating SARS-CoV-2 variants to neutralization. N. Engl. J. Med. *384*, 2354–2356. https://doi.org/10.1056/NEJMc2103022.
8. Altmann, D.M., Boyton, R.J., and Beale, R. (2021). Immunity to SARS-CoV-2 variants of concern. Science *371*, 1103–1104. https://doi.org/10.1126/science.abg7404.
9. Wang, K., Jia, Z., Bao, L., Wang, L., Cao, L., Chi, H., Hu, Y., Li, Q., Zhou, Y., Jiang, Y., et al. (2022). Memory B cell repertoire from triple vaccinees against diverse SARS-CoV-2 variants. Nature *603*, 919–925. https://doi.org/10.1038/s41586-022-04466-x.
10. Schmidt, F., Weisblum, Y., Rutkowska, M., Poston, D., DaSilva, J., Zhang, F., Bednarski, E., Cho, A., Schaefer-Babajew, D.J., Gaebler, C., et al. (2021). High genetic barrier to SARS-CoV-2 polyclonal neutralizing antibody escape. Nature *600*, 512–516. https://doi.org/10.1038/s41586-021-04005-0.
11. Cao, Y., Wang, J., Jian, F., Xiao, T., Song, W., Yisimayi, A., Huang, W., Li, Q., Wang, P., An, R., et al. (2022). Omicron escapes the majority of existing SARS-CoV-2 neutralizing antibodies. Nature *602*, 657–663. https://doi.org/10.1038/s41586-021-04385-3.
12. Liu, L., Iketani, S., Guo, Y., Chan, J.F.W., Wang, M., Liu, L., Luo, Y., Chu, H., Huang, Y., Nair, M.S., et al. (2022). Striking antibody evasion manifested by the Omicron variant of SARS-CoV-2. Nature *602*, 676–681. https://doi.org/10.1038/s41586-021-04388-0.
13. Zhou, T., Wang, L., Misasi, J., Pegu, A., Zhang, Y., Harris, D.R., Olia, A.S., Talana, C.A., Yang, E.S., Chen, M., et al. (2022). Structural basis for potent antibody neutralization of SARS-CoV-2 variants including B.1.1.529. Science, eabn8897. https://doi.org/10.1126/science.abn8897.
14. Cameroni, E., Bowen, J.E., Rosen, L.E., Saliba, C., Zepeda, S.K., Culap, K., Pinto, D., VanBlargan, L.A., De Marco, A., di Iulio, J., et al. (2022). Broadly neutralizing antibodies overcome SARS-CoV-2 Omicron antigenic shift. Nature *602*, 664–670. https://doi.org/10.1038/s41586-021-04386-2.
15. Cele, S., Jackson, L., Khoury, D.S., Khan, K., Moyo-Gwete, T., Tegally, H., San, J.E., Cromer, D., Scheepers, C., Amoako, D.G., et al. (2022). Omicron extensively but incompletely escapes Pfizer BNT162b2 neutralization. Nature *602*, 654–656. https://doi.org/10.1038/s41586-021-04387-1.
16. Carreño, J.M., Alshammary, H., Tcheou, J., Singh, G., Raskin, A.J., Kawabata, H., Sominsky, L.A., Clark, J.J., Adelsberg, D.C., Bielak, D.A., et al. (2022). Activity of convalescent and vaccine serum against SARS-CoV-2 Omicron. Nature *602*, 682–688. https://doi.org/10.1038/s41586-022-04399-5.
17. Planas, D., Saunders, N., Maes, P., Guivel-Benhassine, F., Planchais, C., Buchrieser, J., Bolland, W.H., Porrot, F., Staropoli, I., Lemoine, F., et al. (2022). Considerable escape of SARS-CoV-2 Omicron to antibody neutralization. Nature *602*, 671–675. https://doi.org/10.1038/s41586-021-04389-z.
18. Iketani, S., Liu, L., Guo, Y., Liu, L., Chan, J.F.W., Huang, Y., Wang, M., Luo, Y., Yu, J., Chu, H., et al. (2022). Antibody evasion properties of SARS-CoV-2 Omicron sublineages. Nature *604*, 553–556. https://doi.org/10.1038/s41586-022-04594-4.
19. Baum, A., Fulton, B.O., Wloga, E., Copin, R., Pascal, K.E., Russo, V., Giordano, S., Lanza, K., Negron, N., Ni, M., et al. (2020). Antibody cocktail to SARS-CoV-2 spike protein prevents rapid mutational escape seen with individual antibodies. Science *369*, 1014–1018. https://doi.org/10.1126/science.abd0831.
20. Dong, J., Zost, S., Greaney, A., Starr, T.N., Dingens, A.S., Chen, E.C., Chen, R., Case, B., Sutton, R., Gilchuk, P., et al. (2021). Genetic and structural basis for recognition of SARS-CoV-2 spike protein by a two-antibody cocktail. Preprint at bioRxiv. https://doi.org/10.1101/2021.01.27.428529.
21. Li, C., Zhan, W., Yang, Z., Tu, C., Hu, G., Zhang, X., Song, W., Du, S., Zhu, Y., Huang, K., et al. (2022). Broad neutralization of SARS-CoV-2 variants by an inhalable bispecific single-domain antibody. Cell *185*, 1389–1401.e18. https://doi.org/10.1016/j.cell.2022.03.009.
22. Dougan, M., Nirula, A., Azizad, M., Mocherla, B., Gottlieb, R.L., Chen, P., Hebert, C., Perry, R., Boscia, J., Heller, B., et al. (2021). Bamlanivimab plus etesevimab in mild or moderate covid-19. N. Engl. J. Med. *385*, 1382–1392. https://doi.org/10.1056/NEJMoa2102685.
23. Loo, Y.M., McTamney, P.M., Arends, R.H., Abram, M.E., Aksyuk, A.A., Diallo, S., Flores, D.J., Kelly, E.J., Ren, K., Roque, R., et al. (2022). The SARS-CoV-2 monoclonal antibody combination, AZD7442, is protective in nonhuman primates and has an extended half-life in humans. Sci. Transl. Med. *14*, eabl8124. https://doi.org/10.1126/scitranslmed.abl8124.
24. Westendorf, K., Žentelis, S., Wang, L., Foster, D., Vaillancourt, P., Wiggin, M., Lovett, E., van der Lee, R., Hendle, J., Pustilnik, A., et al. (2022). LY-CoV1404 (bebtelovimab) potently neutralizes SARS-CoV-2 variants. Cell Rep. *39*, 110812. https://doi.org/10.1016/j.celrep.2022.110812.
25. Zhou, Y., Liu, Z., Li, S., Xu, W., Zhang, Q., Silva, I.T., Li, C., Wu, Y., Jiang, Q., Liu, Z., et al. (2021). Enhancement versus neutralization by SARS-CoV-2 antibodies from a convalescent donor associates with distinct epitopes on the RBD. Cell Rep. *34*, 108699. https://doi.org/10.1016/j.celrep.2021.108699.
26. Cao, Y., Yisimayi, A., Jian, F., Song, W., Xiao, T., Wang, L., Du, S., Wang, J., Li, Q., Chen, X., et al. (2022). BA.2.12.1, BA.4 and BA.5 escape antibodies elicited by Omicron infection. Nature *608*, 593–602. https://doi.org/10.1038/s41586-022-04980-y.
27. Liu, Z., Xu, W., Chen, Z., Fu, W., Zhan, W., Gao, Y., Zhou, J., Zhou, Y., Wu, J., Wang, Q., et al. (2022). An ultrapotent pan-beta-coronavirus lineage B (beta-CoV-B) neutralizing antibody locks the receptor-binding domain in closed conformation by targeting its conserved epitope. Protein Cell *13*, 655–675. https://doi.org/10.1007/s13238-021-00871-6.
28. Muecksch, F., Weisblum, Y., Barnes, C.O., Schmidt, F., Schaefer-Babajew, D., Lorenzi, J.C.C., Flyak, A.I., DeLaitsch, A.T., Huey-Tubman, K.E., Hou, S., et al. (2021). Development of potency, breadth and resilience to viral escape mutations in SARS-CoV-2 neutralizing antibodies. Preprint at bioRxiv. https://doi.org/10.1101/2021.03.07.434227.
29. Gaebler, C., Wang, Z., Lorenzi, J.C.C., Muecksch, F., Finkin, S., Tokuyama, M., Cho, A., Jankovic, M., Schaefer-Babajew, D., Oliveira, T.Y.,

et al. (2021). Evolution of antibody immunity to SARS-CoV-2. Nature *591*, 639–644. https://doi.org/10.1038/s41586-021-03207-w.

30. Sokal, A., Chappert, P., Barba-Spaeth, G., Roeser, A., Fourati, S., Azzaoui, I., Vandenberghe, A., Fernandez, I., Meola, A., Bouvier-Alias, M., et al. (2021). Maturation and persistence of the anti-SARS-CoV-2 memory B cell response. Cell *184*, 1201–1213.e14. https://doi.org/10.1016/j.cell.2021.01.050.
31. Yuan, M., Wang, Y., Lv, H., Tan, T.J.C., Wilson, I.A., and Wu, N.C. (2022). Molecular analysis of a public cross-neutralizing antibody response to SARS-CoV-2. Cell Rep. *41*, 111650. https://doi.org/10.1016/j.celrep.2022.111650.
32. Waterhouse, A., Bertoni, M., Bienert, S., Studer, G., Tauriello, G., Gumienny, R., Heer, F.T., de Beer, T.A.P., Rempfer, C., Bordoli, L., et al. (2018). SWISS-MODEL: homology modelling of protein structures and complexes. Nucleic Acids Res. *46*, W296–W303. https://doi.org/10.1093/nar/gky427.
33. Buchanan, A., Clementel, V., Woods, R., Harn, N., Bowen, M.A., Mo, W., Popovic, B., Bishop, S.M., Dall'Acqua, W., Minter, R., et al. (2013). Engineering a therapeutic IgG molecule to address cysteinylation, aggregation and enhance thermal stability and expression. mAbs *5*, 255–262. https://doi.org/10.4161/mabs.23392.
34. Fang, Y., Sun, P., Xie, X., Du, M., Du, F., Ye, J., Kalveram, B.K., Plante, J.A., Plante, K.S., Li, B., et al. (2022). An antibody that neutralizes SARS-CoV-1 and SARS-CoV-2 by binding to a conserved spike epitope outside the receptor binding motif. Sci. Immunol. *7*, eabp9962. https://doi.org/10.1126/sciimmunol.abp9962.
35. Pinto, D., Park, Y.J., Beltramello, M., Walls, A.C., Tortorici, M.A., Bianchi, S., Jaconi, S., Culap, K., Zatta, F., De Marco, A., et al. (2020). Cross-neutralization of SARS-CoV-2 by a human monoclonal SARS-CoV antibody. Nature *583*, 290–295. https://doi.org/10.1038/s41586-020-2349-y.
36. Nutalai, R., Zhou, D., Tuekprakhon, A., Ginn, H.M., Supasa, P., Liu, C., Huo, J., Mentzer, A.J., Duyvesteyn, H.M.E., Dijokaite-Guraliuc, A., et al. (2022). Potent cross-reactive antibodies following Omicron breakthrough in vaccinees. Cell *185*, 2116–2131.e18. https://doi.org/10.1016/j.cell.2022.05.014.
37. VanBlargan, L.A., Errico, J.M., Halfmann, P.J., Zost, S.J., Crowe, J.E., Jr., Purcell, L.A., Kawaoka, Y., Corti, D., Fremont, D.H., and Diamond, M.S. (2022). An infectious SARS-CoV-2 B.1.1.529 Omicron virus escapes neutralization by therapeutic monoclonal antibodies. Nat. Med. *28*, 490–495. https://doi.org/10.1038/s41591-021-01678-y.
38. Kramer, K.J., Johnson, N.V., Shiakolas, A.R., Suryadevara, N., Periasamy, S., Raju, N., Williams, J.K., Wrapp, D., Zost, S.J., Walker, L.M., et al. (2021). Potent neutralization of SARS-CoV-2 variants of concern by an antibody with an uncommon genetic signature and structural mode of spike recognition. Cell Rep. *37*, 109784. https://doi.org/10.1016/j.celrep.2021.109784.
39. Wang, K., Jia, Z., Bao, L., Wang, L., Cao, L., Chi, H., Hu, Y., Li, Q., Zhou, Y., Jiang, Y., et al. (2022). Memory B cell repertoire from triple vaccinees against diverse SARS-CoV-2 variants. Nature *603*, 919–925. https://doi.org/10.1038/s41586-022-04466-x.
40. Xia, S., Liu, M., Wang, C., Xu, W., Lan, Q., Feng, S., Qi, F., Bao, L., Du, L., Liu, S., et al. (2020). Inhibition of SARS-CoV-2 (previously 2019-nCoV) infection by a highly potent pan-coronavirus fusion inhibitor targeting its spike protein that harbors a high capacity to mediate membrane fusion. Cell Res. *30*, 343–355. https://doi.org/10.1038/s41422-020-0305-x.
41. Ye, J., Ma, N., Madden, T.L., and Ostell, J.M. (2013). IgBLAST: an immunoglobulin variable domain sequence analysis tool. Nucleic Acids Res. *41*, W34–W40. https://doi.org/10.1093/nar/gkt382.
42. Brochet, X., Lefranc, M.P., and Giudicelli, V. (2008). IMGT/V-QUEST: the highly customized and integrated system for IG and TR standardized V-J and V-D-J sequence analysis. Nucleic Acids Res. *36*, W503–W508. https://doi.org/10.1093/nar/gkn316.
43. Pettersen, E.F., Goddard, T.D., Huang, C.C., Couch, G.S., Greenblatt, D.M., Meng, E.C., and Ferrin, T.E. (2004). UCSF Chimera–a visualization system for exploratory research and analysis. J. Comput. Chem. *25*, 1605–1612. https://doi.org/10.1002/jcc.20084.
44. Sanchez-Garcia, R., Gomez-Blanco, J., Cuervo, A., Carazo, J.M., Sorzano, C.O.S., and Vargas, J. (2021). DeepEMhancer: a deep learning solution for cryo-EM volume post-processing. Commun. Biol. *4*, 874. https://doi.org/10.1038/s42003-021-02399-1.
45. Wang, Q., Michailidis, E., Yu, Y., Wang, Z., Hurley, A.M., Oren, D.A., Mayer, C.T., Gazumyan, A., Liu, Z., Zhou, Y., et al. (2020). A combination of human broadly neutralizing antibodies against hepatitis B virus HBsAg with distinct epitopes suppresses escape mutations. Cell Host Microbe *28*, 335–349.e6. https://doi.org/10.1016/j.chom.2020.05.010.
46. Zhou, Y., Liu, Z., Wang, Z., Zhang, Q., Mayer, C.T., Schoofs, T., Nussenzweig, M.C., de Jong, Y.P., and Wang, Q. (2020). Single-cell sorting of HBsAg-binding memory B cells from human peripheral blood mononuclear cells and antibody cloning. STAR Protoc. *1*, 100129. https://doi.org/10.1016/j.xpro.2020.100129.
47. Mastronarde, D.N. (2005). Automated electron microscope tomography using robust prediction of specimen movements. J. Struct. Biol. *152*, 36–51. https://doi.org/10.1016/j.jsb.2005.07.007.
48. Wu, C., Huang, X., Cheng, J., Zhu, D., and Zhang, X. (2019). High-quality, high-throughput cryo-electron microscopy data collection via beam tilt and astigmatism-free beam-image shift. J. Struct. Biol. *208*, 107396. https://doi.org/10.1016/j.jsb.2019.09.013.
49. Zheng, S.Q., Palovcak, E., Armache, J.P., Verba, K.A., Cheng, Y., and Agard, D.A. (2017). MotionCor2: anisotropic correction of beam-induced motion for improved cryo-electron microscopy. Nat. Methods *14*, 331–332. https://doi.org/10.1038/nmeth.4193.
50. Zivanov, J., Nakane, T., Forsberg, B.O., Kimanius, D., Hagen, W.J., Lindahl, E., and Scheres, S.H. (2018). New Tools for Automated High-Resolution Cryo-EM Structure Determination in RELION-3. Elife *7*. https://doi.org/10.7554/eLife.42166.
51. Zhang, K. (2016). Gctf: real-time CTF determination and correction. J. Struct. Biol. *193*, 1–12. https://doi.org/10.1016/j.jsb.2015.11.003.
52. Punjani, A., Rubinstein, J.L., Fleet, D.J., and Brubaker, M.A. (2017). cryoSPARC: algorithms for rapid unsupervised cryo-EM structure determination. Nat. Methods *14*, 290–296. https://doi.org/10.1038/nmeth.4169.
53. Asarnow, D., Palovcak, E., and Cheng, Y. (2019). UCSF Pyem v0.5, Zenodo. https://doi.org/10.5281/zenodo.3576630.
54. Emsley, P., Lohkamp, B., Scott, W.G., and Cowtan, K. (2010). Features and development of coot. Acta Crystallogr. D Biol. Crystallogr. *66*, 486–501. https://doi.org/10.1107/S0907444910007493.
55. Afonine, P.V., Poon, B.K., Read, R.J., Sobolev, O.V., Terwilliger, T.C., Urzhumtsev, A., and Adams, P.D. (2018). Real-space refinement in PHENIX for cryo-EM and crystallography. Acta Crystallogr. D Struct. Biol. *74*, 531–544. https://doi.org/10.1107/S2059798318006551.
56. Pettersen, E.F., Goddard, T.D., Huang, C.C., Meng, E.C., Couch, G.S., Croll, T.I., Morris, J.H., and Ferrin, T.E. (2021). UCSF ChimeraX: structure visualization for researchers, educators, and developers. Protein Sci. *30*, 70–82.

STAR★METHODS

KEY RESOURCES TABLE

REAGENT or RESOURCE	SOURCE	IDENTIFIER
Antibodies		
XG anti-SARS-CoV-2 bNAbs	Zhou et al.[25]	N/A
XG005a	This paper	N/A
XG005b	This paper	N/A
XG005c	This paper	N/A
Ly-CoV1404	Westendorf et al.[24]	N/A
Goat anti-Human IgG (H + L) secondary antibody, HRP	Thermo Fisher Scientific	Cat#31410; RRID: AB_228269
Bacterial and virus strains		
E. Coli trans5α chemically Competent Cells	TransGen Biotech	Cat#CD201-01
Authentic BA.2 and BA.5 virus	Guangzhou Custom Technology Center	N/A
Chemicals, peptides, and recombinant proteins		
SARS-CoV-2 Spike protein (ECD, His & FLAG tag)	GenScript	Cat#Z03481
SARS-CoV-2 variant proteins (ECD)	Wang et al.[39]	N/A
SARS-CoV-2 Omicron S trimer	This paper	N/A
PBS (10×), pH 7.2–7.4	Solarbio Life Sciences	Cat#P1022
1 M Tris-HCl, pH 9.0	Solarbio Life Sciences	Cat#T1160
Dimethyl Sulfoxide	Sigma	Cat#2650
Bovine Serum Albumin	WeiAo Biotech, Shanghai	Cat#WH3044
Fetal Bovine Serum	GEMINI	Cat#900-108
OPM-293 CD05	OPM biosciences	Cat# 81075-001
OPM-293 PreFeed	OPM biosciences	Cat#F081919-001
DPBS	VivaCell	Cat#C3590-0500
Opti-MEM	Gibco	Cat#31985070
SurePAGE™	Genscript	Cat#M00654
Tris-MOPS-SDS	Genscript	Cat#M00138
5× Protein loading buffer	Genscript	Cat#MB01015
Protein Marker	Genscript	Cat#M00624
InstaBlue Protein Stain Solution	APExBIO	Cat#B8226
ABTS Chromogen/substrate solution for ELISA	Thermo Fisher Scientific	Cat#00-2024
EZ *trans*	Life iLab Biotech Co., Ltd, Shanghai, China	Cat#AC04L082
Critical commercial assays		
Superose 6 Increase 10/300 column	GE Healthcare	Cat#CA10192-228
Histrap HP	GE Healthcare	Cat#17-5248-02
Protein G Sepharose 4 Fast Flow	GE Healthcare	Cat#17061805
Pierce™ IgG Elution buffer	Thermo Scientific	Cat#21004
AgeI-HF	New England BioLabs	Cat#R3552L
BsiwI-HF	New England BioLabs	Cat#R3553L
BamH1	New England BioLabs	Cat# R0136M
XhoI	New England BioLabs	Cat#R0146L
SalI-HF	New England BioLabs	Cat#R3138S
10× NEB buffer 2	New England BioLabs	Cat#B7002S

(*Continued on next page*)

Continued

REAGENT or RESOURCE	SOURCE	IDENTIFIER
Phusion High-Fidelity DNA Polymerase	Thermo Scientific	Cat#M0530L
T4 DNA polymerase	New England BioLabs	Cat#M0203L
T4 DNA ligase	New England BioLabs	Cat#M0202M
NucleoSpin Gel and PCR Clean-up	New England BioLabs	Cat#740690.250
Luciferase Cell Culture Lysis 5× Reagent	Promega	Cat#E1531
Firefly Luciferase Assay Kit	Promega	Cat#E1501
VigoFect	Vigorous Biotechnology	Cat#T001
HiPure Plasmid EF Maxi Kit	Magen	Cat#P1156
Deposited data		
SARS-CoV-2 wild-type S trimer-XG005 fab complex structure	Liu et al.[27]	PDB: 7V26
SARS-CoV-2 Omicron S trimer-XG005 fab complex structure	This paper	PDB: 7YD0, 7YCY, 7YCZ, 7YD1
Experimental models: Cell lines		
HEK293F cell line	Zhou et al.[25]	N/A
HEK293T cell line	Xia et al.[40]	N/A
Huh-7 cell line	Xia et al.[40]	N/A
Raji cell line	Zhou et al.[25]	N/A
Vero-E6 cell line	Guangzhou Custom Technology Center	N/A
Experimental models: Organisms/strains		
Human ACE2 transgenic mice	GuangDong GemPharmatech Co., Ltd.	N/A
C57BL/6JSmoc hFcRn transgenic mice	Shanghai Model Organisms Center, China	N/A
Recombinant DNA		
pNL4-3.luc.RE	Xia et al.[40]	N/A
pcDNA3.1-SARS-CoV-1-S	Xia et al.[40]	N/A
pcDNA3.1-SARS-COV-2-S	Xia et al.[40]	N/A
pcDNA3.1-SARS-CoV-2-S mutants	This paper	N/A
Software and algorithms		
PRISM	GraphPad	https://www.graphpad.com
IgBlast	Ye et al.[41]	http://www.ncbi.nlm.nih.gov/igblast/
IMGT/V-QUEST	Brochet et al.[42]	http://www.imgt.org/IMGT_vquest/vquest
FMSB	R project	http://www.r-project.org
Swiss-model	Waterhouse et al.[32]	https://swissmodel.expasy.org
UCSF Chimera	Pettersen et al.[43]	https://www.cgl.uscf.edu/chimera/
DeepEMhancer	Sanchez-Garcia et al.[44]	https://github.com/rsanchezgarc/deepEMhancer
Others		
Sterile 50 mL Disposable Vacuum Filtration System	Millipore Sigma	Cat#SCGP00525
Amicon Ultra-4 Centrifugal Filters Ultracel-30K	Merck Millipore Ltd.	Cat#UFC803096
Ultrafree-MC Centrifugal filter units, 0.22uM GV DURAPORE	Merck Millipore Ltd.	Cat#UFC30GV0S
General Long-Term Storage Cryogenic Tubes	Nalgene	Cat#5000-1020
SimpliAmp™ Thermal Cycler	Thermo Fisher Scientific	Cat#A24812
500 mL Bottle Top Vacuum Filter, 0.20 μm Pore	Thermo Fisher Scientific	Cat#566-0020
ACCUSPIN Tubes Sterile, 50mL Capacity	Sigma	Cat#A2055-10EA

RESOURCE AVAILABILITY

Lead contact

Further information and requests for resources and reagents should be directed to and will be fulfilled by the lead contact, Qiao Wang (wangqiao@fudan.edu.cn).

Materials availability

All unique reagents generated in this study are available from the lead contact with a completed Materials Transfer Agreement. Sharing of antibodies with academic researchers may require a payment to cover the cost of generation and a completed Material Transfer Agreement.

Data and code availability

- Data reported in this paper will be shared by the lead contact upon request. The XG005-related complex structures (PDB accession numbers: 7V26, 7YD0, 7YCY, 7YCZ, 7YD1) reported in this paper are publicly available as of the date of publication.
- This paper does not report original code.
- Any additional information required to reanalyze the data reported in this paper is available from the lead contact upon request.

EXPERIMENTAL MODEL AND SUBJECT DETAILS

For therapeutic study, transgenic mice with human ACE2 overexpression (K18-hACE2_C57BL/6J) were purchased from Guangdong GemPharmatech Co., Ltd., and all mice used in this study were 6–8 weeks old and only male mice were used. For pharmacokinetic study, transgenic mice (C57BL/6JSmoc-Fcgrt$^{em2(hFCGRT)Smoc}$) with human neonatal Fc receptor (hFcRn) overexpression were purchased from Shanghai Model Organisms Center, and all mice used were female and 8–10 weeks old. Experiments related to animals were conducted according to institutional regulations of Basic Medical School of Fudan University. Human HEK293T, HEK293F, Huh-7 cells, Vero-E6, and Raji cells were maintained as previously reported.[25] All cell lines were cultured at 37 °C with 5% CO_2, while HEK293F were cultured using serum-free OPM-293-CD05 medium (OPM Biosciences) with shaking at 100 rpm.

METHOD DETAILS

ELISA

To perform ELISA, 96-well microplates were coated with antigen proteins (10 μg/mL) in phosphate-buffered saline (PBS) (50 μL per well) overnight at 4 °C. Antigen proteins were S-ECD protein of SARS-CoV-2 Wuhan-Hu-1 (wild-type) and its related variants, including Alpha (B.1.1.7), Beta (B.1.351), Gamma (P.1), Delta (B.1.617.2) and Omicron (B.1.1.529). These coated plates were then blocked with PBS containing 2% bovine serum albumin (BSA) (200 μL per well). After blocking, the plate was incubated with the first antibody (eight dilutions with a maximum concentration of 10 μg/mL, 3-fold serially diluted) in PBS (50 μL per well) for 1 h at room temperature. After wash, the second antibody (goat anti-human IgG conjugated with HRP, Thermo Fisher Scientific) in PBS (50 μL per well) was added to each well for another 1-h incubation, and then detection was performed. To evaluate the antigen-binding capacity, we calculated the area under the curve (AUC) for each purified recombinant IgG1 mAb using PRISM software as previously reported.[45]

Generation of SARS-CoV-1/2 pseudoviruses

Pseudotyped viruses of SARS-CoV-1, SARS-CoV-2 and SARS-CoV-2-related variants were generated as described previously.[25,40] We first constructed the S-protein expression plasmids pcDNA3.1-SARS-CoV-2-S or pcDNA3.1-SARS-CoV-1-S. The S protein amino acid sequences for SARS-CoV-2 wild-type and variants were provided (Table S2). We then co-transfected the constructed pcDNA3.1 plasmids with the backbone plasmid of pNL4-3.Luc.R-E into HEK293T cells. Two days later, we collected the cell supernatants containing pseudoviruses and stored them at −80 °C for *in vitro* neutralization assays.

In vitro pseudotyped virus-based neutralization assay for SARS-CoV-2

We performed the *in vitro* pseudovirus neutralization assays as previously described (Xia et al., 2020; Zhou et al., 2021). We first examined the generated pseudotyped viruses by infecting Huh-7 cells and measuring luciferase activity to determine the virus concentration. We then aliquoted the concentrated virus stock and stored it at −80 °C. To perform the *in vitro* neutralization experiments, we seeded Huh-7 cells in 96-well plates (10^4 cells per well) and serially diluted (1:3) the overexpressed mAbs (maximum concentration 10 μg/mL) for nine dilutions in total. We mixed and incubated the antibody soup and concentrated pseudovirus soup for 30 min at 37 °C, and then added them into the Huh-7 cells for 24 h of incubation. We then replated the cell supernatant with fresh DMEM containing 10% FBS and collected cells after 36 h of cell culture. Finally, we lysed the cultured cells and measured luciferase activity using a Firefly Luciferase Assay Kit (Promega, USA) and a microplate reader (Infinite M200PRO, Switzerland) following the manufacturer's instructions. Due to the dramatic variation of the absolute luciferase values, we calculated the relative luminescence values by

normalizing them to pseudovirus-only control wells. The IC_{50} values by neutralization assays were calculated by nonlinear regression analysis in PRISM software.

In vitro neutralization assay using authentic BA.2 and BA.5 viruses

Experiments including viral amplification and viral infection were conducted in a Biosafety Level 3 (BSL-3) laboratory. The authentic BA.2 and BA.5 viruses were amplified and titered in Vero-E6 cells using the plaque assay. The *in vitro* neutralization assay was performed as described previously.[25,27] Different concentrations of mAbs were mixed with the authentic BA.2 or BA.5 viruses for 1 h before adding onto cultured cells. Twenty-four hours later, the cells were fixed and subjected to immunostaining assay to determine the cell infection rate.

Antibody cloning and production

Single B cell-based antibody amplification and sequence analysis were performed as previously reported.[45,46] Briefly, we performed the reverse transcription and nested PCR amplification for the sorted single B cells.[25] We analyzed all the Sanger sequencing results of heavy and light chains and identified the V(D)J gene and CDR3 sequences using IMGT/V-QUEST[42] and/or IgBLAST.[41] For antibody expression, we transiently transfected HEK293F cells with heavy/light chain plasmids and harvested supernatants seven days later for antibody purification.

Expression and purification of SARS-CoV-2 Omicron S trimer

The vector of Omicron S ectodomain with HexaPro mutations, "GSAS" substitution at furin cleavage site (residues 682-285) and a C-terminal T4 fibritin trimerization was constructed as previously reported[21] and transfected into HEK293F cells for expression.

After 72 h, the supernatants were harvested and filtered for affinity purification by Histrap HP (GE Healthcare). The protein was then loaded onto a Superose 6 increase 10/300 column (GE Healthcare) in 20 mM Tris pH 8.0, 200 mM NaCl.

Cryo-EM sample preparation

Purified SARS-CoV-2 Omicron S at 0.60 mg/mL was mixed with XG005 antibody by a molar ratio of 1:1.7 and incubated for 10 min on ice. A 3 μL aliquot of the sample was loaded onto a freshly glow-discharged holey amorphous nickel-titanium alloy film supported by 400 mesh gold grids. The sample was frozen immediately in liquid ethane using Vitrobot IV (FEI/Thermo Fisher), with 2 s blot time and −3 blot force and 10 s wait time.

Cryo-EM data collection and image processing

Cryo-EM data were collected on a Titan Krios microscope (Thermo Fisher) operated at 300 kV. Movies were captured with a K3 summit direct detector (Gatan) after a GIF quantum energy filter (Gatan) setting to a slit width of 20 eV. Automated data acquisition was carried out with SerialEM software[47] through beam-image shift method.[48]

Movies were taken in the super-resolution mode at a nominal magnification 81,000×, corresponding to a physical pixel size of 1.064 Å, and a defocus range from −1.2 μm to −2.5 μm. Each movie stack was dose-fractionated to 40 frames with a total exposure dose of about 58 $e^{-}/Å^{2}$ and exposure time of 3s.

A total of 6,503 movie stacks was motion corrected using MotionCor2[49] within RELION.[50] Parameters of contrast transfer function (CTF) were estimated by using Gctf.[51] All micrographs then were manually selected for further particle picking upon astigmatism, defocus range and estimated resolution.

Remaining 6,098 good images were imported into cryoSPARC[52] for further patched CTF-estimating, blob-picking and 2D classification. Several good 2D classes were used as templates for template-picking. After 2D classification of particles from template-picking was finished, all good particles from blob-picking and template-picking were merged and deduplicated, subsequently being exported back to RELION through pyem package.[53]

Total 2,028,032 particles were extracted at a box-size of 320 and rescaled to 160, then carried on one round of 3D classification in RELION. Only good classes were selected, yielding 1,594,120 particles. These particles were performed other rounds of 3D classification to get different states of trimer. Finally, three main states with clear Fabs were selected out, and their corresponding particles were separately re-extracted (unbinned, 1.064 Å/pixel) and auto-refined, then CTF-refined and polished. 153,541 of state 1 (1-RBD-up with 2 Fabs) was yielding a map at 3.62 Å, 124,608 of state 2 (1-RBD-up with 3 Fabs) was yielding a map at 3.74 Å, and 616,627 of state 3 (2-RBD-up with 3 Fabs) was yielding a map at 3.24 Å.

To get more clear structural information of interface between RBD with Fab, we carried on local 3D-classification focused on the best pair of RBD and Fab from state 3. In final, 313,560 particles were subtracted and exported to cryoSPARC to do local refinement, yielding a 2.99 Å local map.

The reported resolutions above are based on the gold-standard Fourier shell correlation (FSC) 0.143 criterion. The above procedures of data processing are summarized (Figures S3 and S4). These sharpened maps were generated by DeepEMhancer[44] and then "vop zflip" to get the correct handedness in UCSF Chimera[43] for subsequent model building and analysis.

Model building and refinement

For model building of SARS-CoV-2 Omicron S XG005 complex, the SARS-CoV-2 Omicron S trimer model and the antibody model generated by swiss-model[32] were fitted into the map using UCSF Chimera and then manually adjusted with COOT.[54] The interface between RBD and Fab region was refined against the local refinement map and then docked back into the into global refinement trimer maps. Several iterative rounds of real-space refinement were further carried out in PHENIX.[55] Model validation was performed using MolProbity. Figures were prepared using UCSF Chimera and UCSF ChimeraX.[56]

The cryo-EM maps and the coordinates of SARS-CoV-2 Omicron S complexed with XG005 have been deposited to the Electron Microscopy DataBank (EMDB) and Protein DataBank (PDB) with accession numbers EMD-33744 and PDB 7YD0 (state 1, UDD with two Fabs), EMD-33742 and PDB 7YCY (state 2, UDD with three Fabs), EMD-33743 and PDB 7YCZ (state 3, UDU with three Fabs), and EMD-33745 and PDB 7YD1 (Local refinement).

Human ACE2 transgenic mice and *in vivo* studies

Mouse experiments were conducted in a Biosafety Level 3 (BSL-3) laboratory in Guangzhou Custom technology center. Transgenic mice with human ACE2 overexpression (K18-hACE2_C57BL/6J) were randomly assigned to distinct groups. A single administration of mAbs (or an equal volume of PBS as a negative control) was administered intraperitoneally 4 h after all mice were intranasally challenged with 10^5 PFU BA.2 or BA.5 authentic viruses. Mouse body weight was monitored, and lungs were collected two days post-infection to determine the live viral loads in lungs by the focus forming assay (FFA).

Pharmacokinetic analysis

Transgenic mice with human neonatal Fc receptor (hFcRn) overexpression (C57BL/6JSmoc-Fcgrt$^{em2(hFCGRT)Smoc}$) (Vendor: Shanghai Model Organisms Center, China) were used to evaluate the pharmacokinetic profiles of mAbs XG005, XG005-CYLK, and LY-CoV1404 (bebtelovimab). Twenty-seven mice were randomly assigned into three groups and a single dose of mAbs (10 mg/kg) were administrated based on their body weights. The serums samples were collected on different time points, including -1-day pre-infusion and 2, 4, 8, 24, 48, 96, 168, 240, 336, 504, 672, 840 h post-infusion. Sample analysis was conducted utilizing validated ELISA methods. Sample concentration data was collected on the INFINITE 200 PRO plate reader and processed using INFINITE 200 PRO Software (2013) Tecan. Pharmacokinetic parameters were evaluated using a non-compartmental approach with Phoenix WinNonlin software (Version 8.0.0.3176, Pharsight, CA).

QUANTIFICATION AND STATISTICAL ANALYSIS

The detailed information of analysis could be found in the Result and Figure Legends. The area under the ELISA curves (ELISA AUC) and the 50% inhibitory concentration (IC_{50}) values calculated for antibody neutralization capacities were calculated in PRISM software.

Cell Reports, Volume *42*

Supplemental information

Fortuitous somatic mutations during antibody evolution endow broad neutralization against SARS-CoV-2 Omicron variants

Jianbo Wu, Zhenguo Chen, Yidan Gao, Zegen Wang, Jiarong Wang, Bing-Yu Chiang, Yunjiao Zhou, Yuru Han, Wuqiang Zhan, Minxiang Xie, Weiyu Jiang, Xiang Zhang, Aihua Hao, Anqi Xia, Jiaying He, Song Xue, Christian T. Mayer, Fan Wu, Bin Wang, Lunan Zhang, Lei Sun, and Qiao Wang

SUPPLEMENTARY FIGURES AND LEGENDS

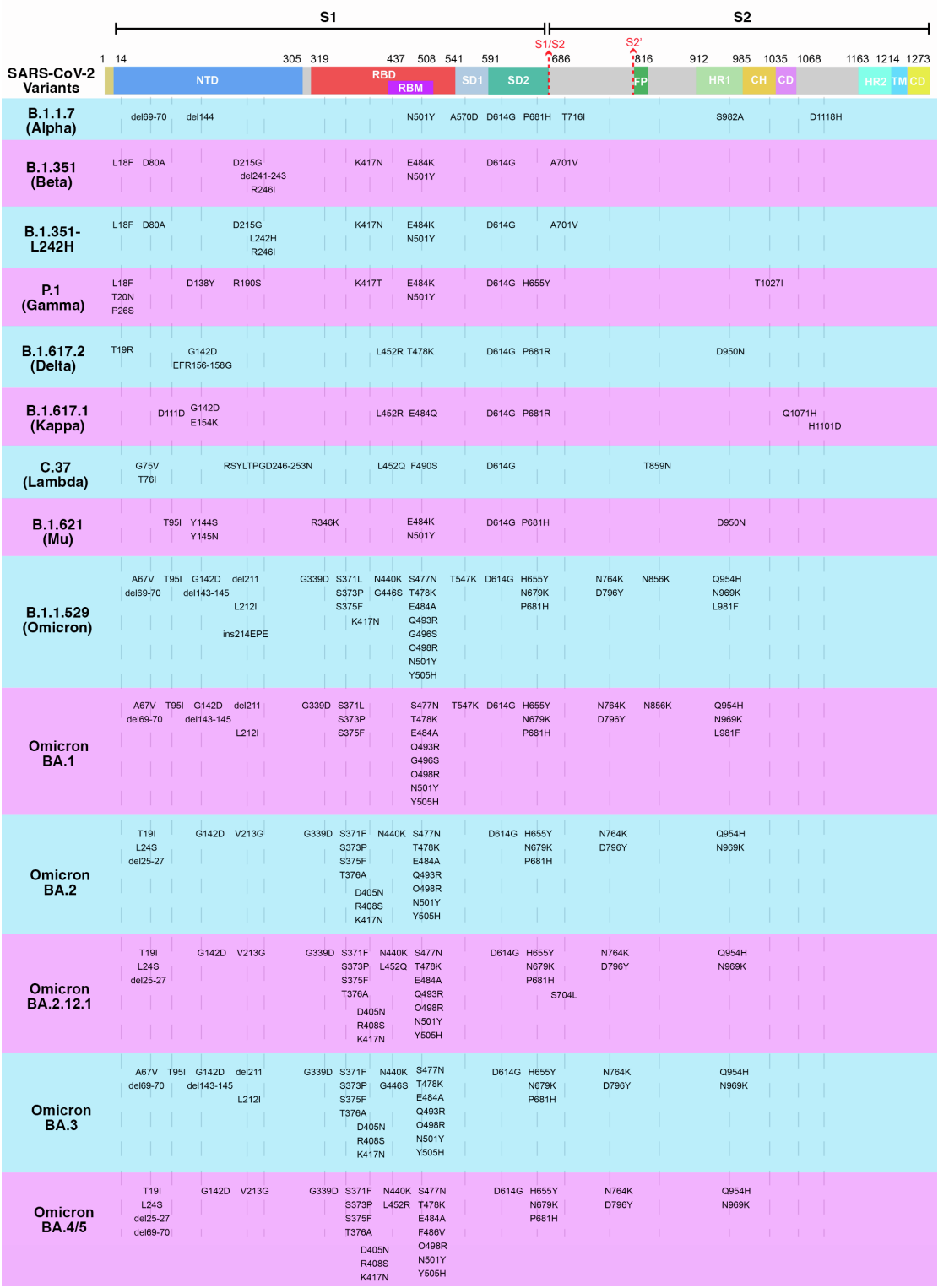

Figure S1. S protein mutations within SARS-CoV-2 variants. Related to Figure 1.

Key spike mutations found in the SARS-CoV-2 variants, compared with Wuhan-Hu-1 (wild-type), are denoted. These variants include five SARS-CoV-2 VOCs: B.1.1.7 (Alpha), B.1.351 (Beta), P.1 (Gamma), B.1.617.2 (Delta) and B.1.1.529 (Omicron); five Omicron variants: BA.1, BA.2, BA.2.12.1, BA.3 and BA.4/5; and four other variants: B.1.351-L242H, B.1.617.1 (Kappa), C.37 (Lambda) and B.1.621 (Mu).

Figure S2. Spider charts for IC_{50} values of 45 mAbs. Related to Figure 2.

IC_{50} values against Wuhan-Hu-1 (wild-type), B.1.1.7 (Alpha), B.1.351 (Beta), P.1 (Gamma), B.1.617.2 (Delta) and B.1.1.529 (Omicron) pseudoviruses were measured for all 45 tested antibodies isolated from a convalescent donor (Zhou et al., 2021). Antibodies with IC_{50} values (mean of two independent experiments.) above 10 μg/ml were shown as 10 μg/ml.

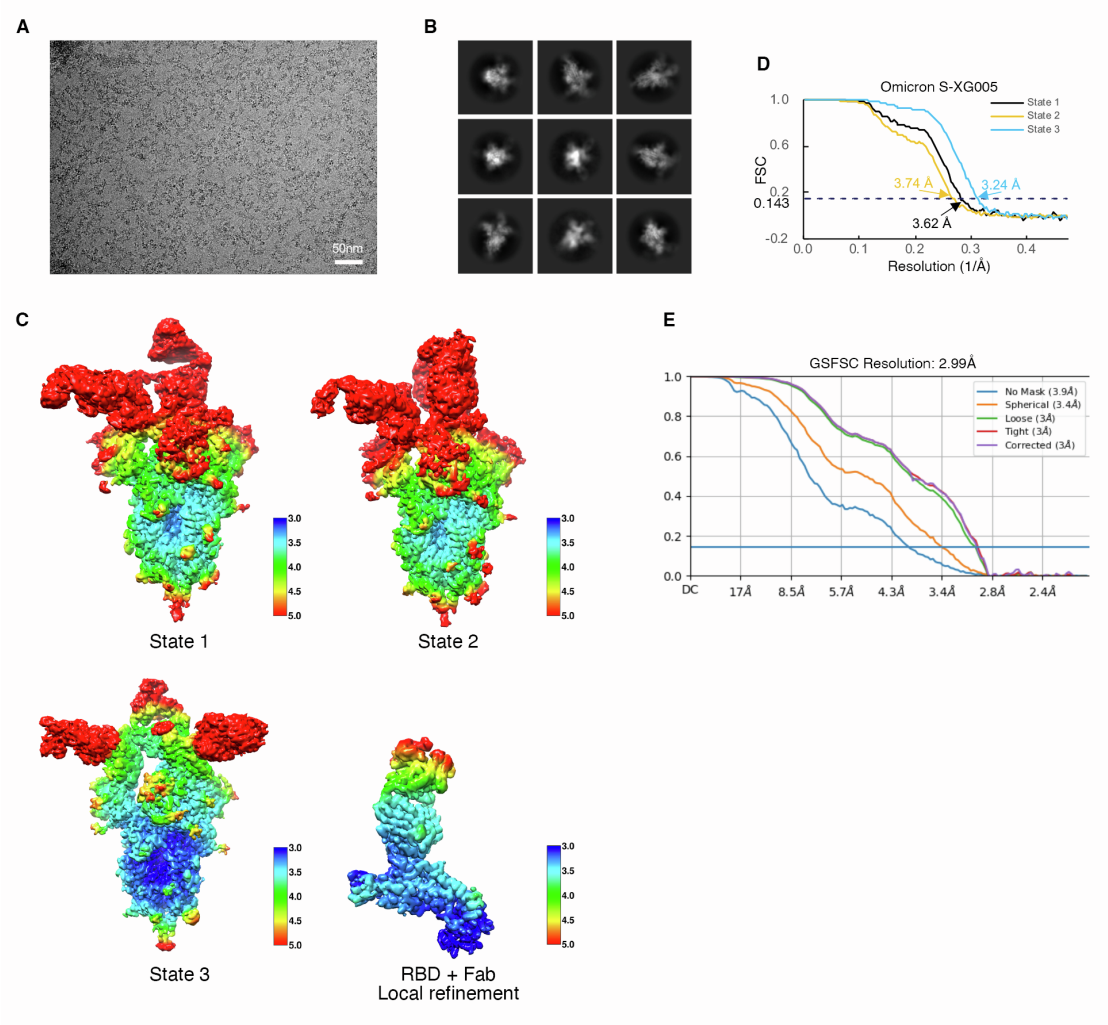

Figure S3. Cryo-EM data collection and processing of Omicron S-XG005 complex (OS-XG005). Related to Figure 3.

(A) Representative electron micrograph.

(B) 2D classification results of OS-XG005.

(C) Local resolution of the reconstruction maps generated by DeepEMhancer.

(D) Gold-standard Fourier shell correlation curves (FSC) for each structure. The 0.143 cut-off is indicated by a horizontal dashed line.

(E) FSC of local refinement of RBD-XG005 Fab region obtained from cryoSPARC.

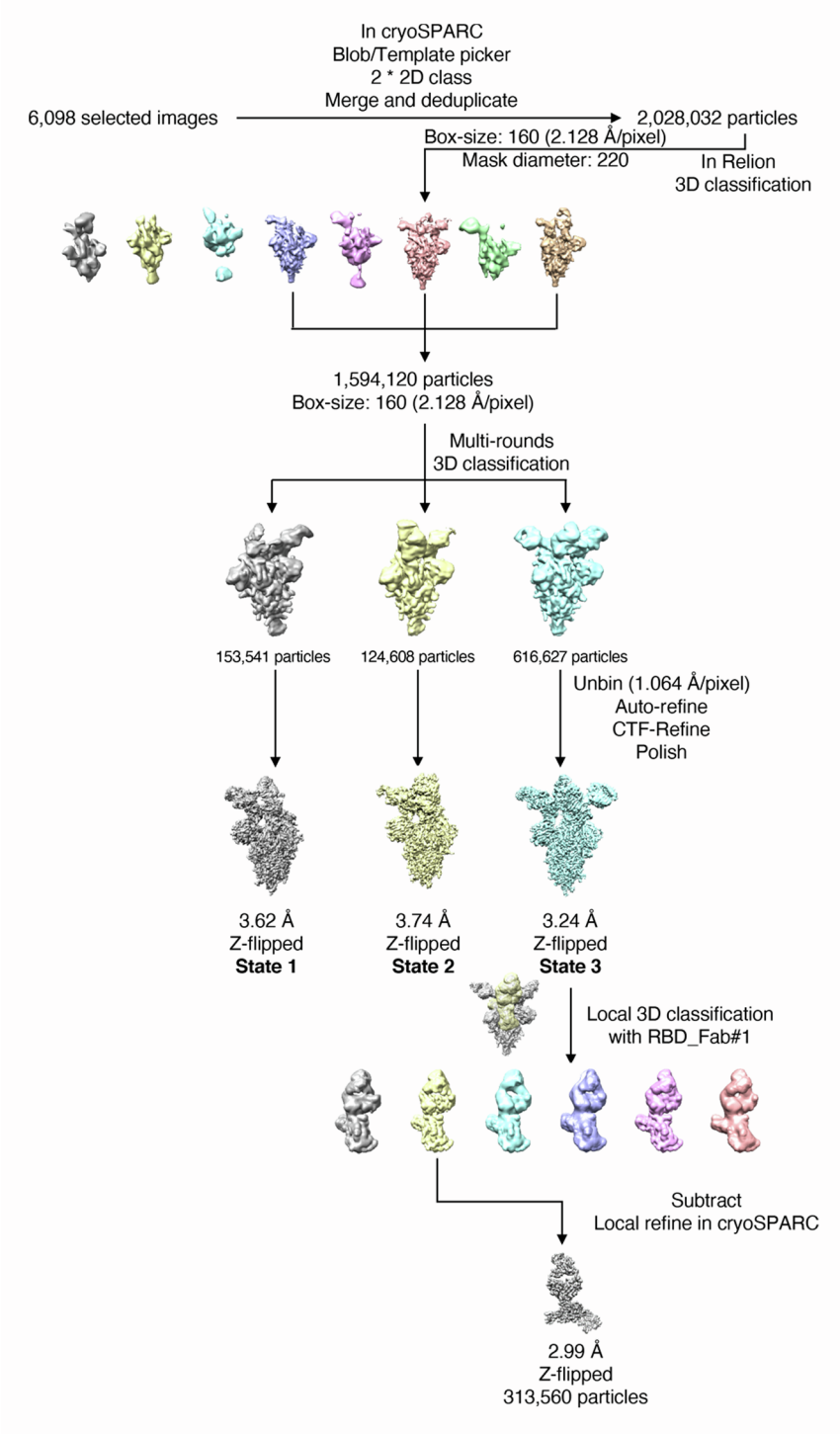

Figure S4. Data processing flowchart of OS-XG005 complex. Related to Figure 3.

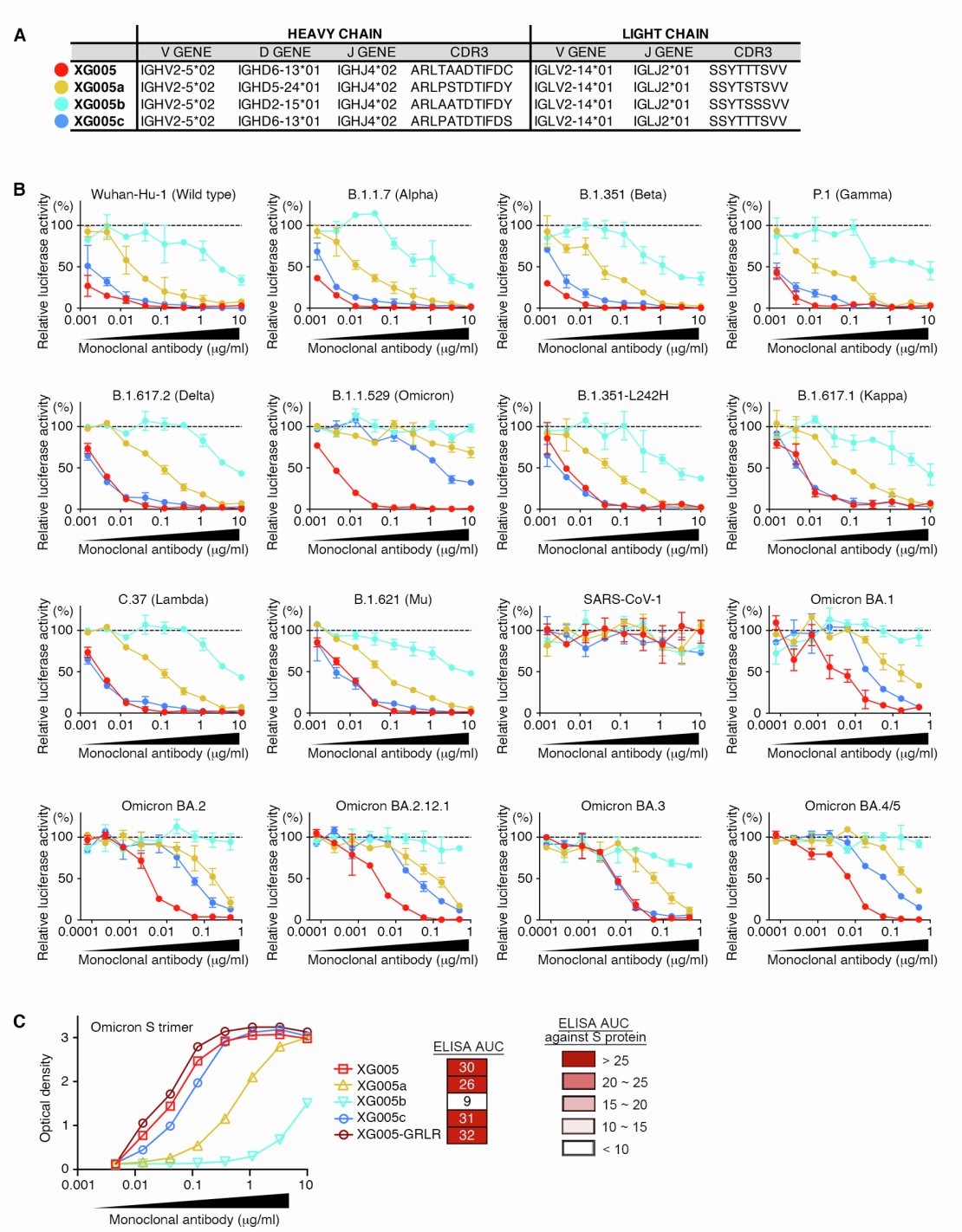

Figure S5. In vitro pseudovirus neutralization assays for XG005 family members. Related to Figure 5.

(A) V(D)J assignments for the XG005 clone. IMGT/V-QUEST was used to assign the V, D, J genes and CDR3 sequences for their Ig heavy and light chains.

(B) Neutralization potency of XG005 family members. Luciferase-based pseudoviruses were used for in vitro infection. Dashed line represents no antibody control. All experiments were repeated at least twice, presented as mean ± SEM.

(C) Dramatically distinct binding capacity against Omicron S protein by XG005 family members. ELISA assays to determine the antibody binding capacity against Omicron S proteins. ELISA area under the curve (AUC) values were calculated. XG005c showed similar level of binding activity of XG005, while those of XG005b and XG005c dramatically reduced.

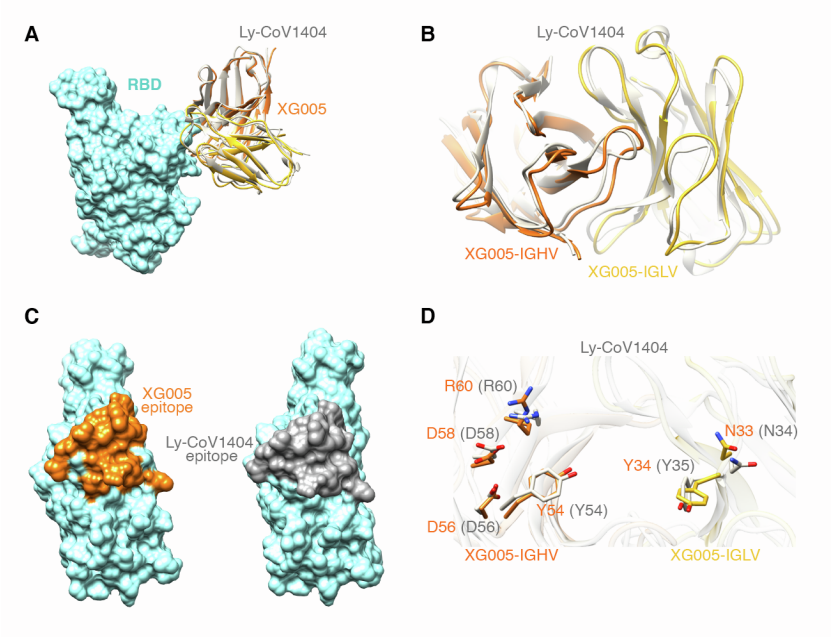

Figure S6. Structural comparison between XG005 and LY-CoV1404. Related to Figure 5.

(A) Comparison the models of wild-type RBD complexed with XG005 and LY-CoV1404. RBD is displayed in sky-blue surface; XG005 heavy and light chains are shown in orange and yellow ribbons, respectively, while LY-CoV1404 is shown in gray.

(B) A close view of XG005 and LY-CoV1404.

(C) Surface representation of RBD showing the interfaces of XG005 (orange) and LY-CoV1404 (dark gray), respectively.

(D) Comparison of the key residues of XG005 and LY-CoV1404 involved in the RBD interaction. Residues of XG005 and LY-CoV1404 are labeled in orange and gray, respectively.

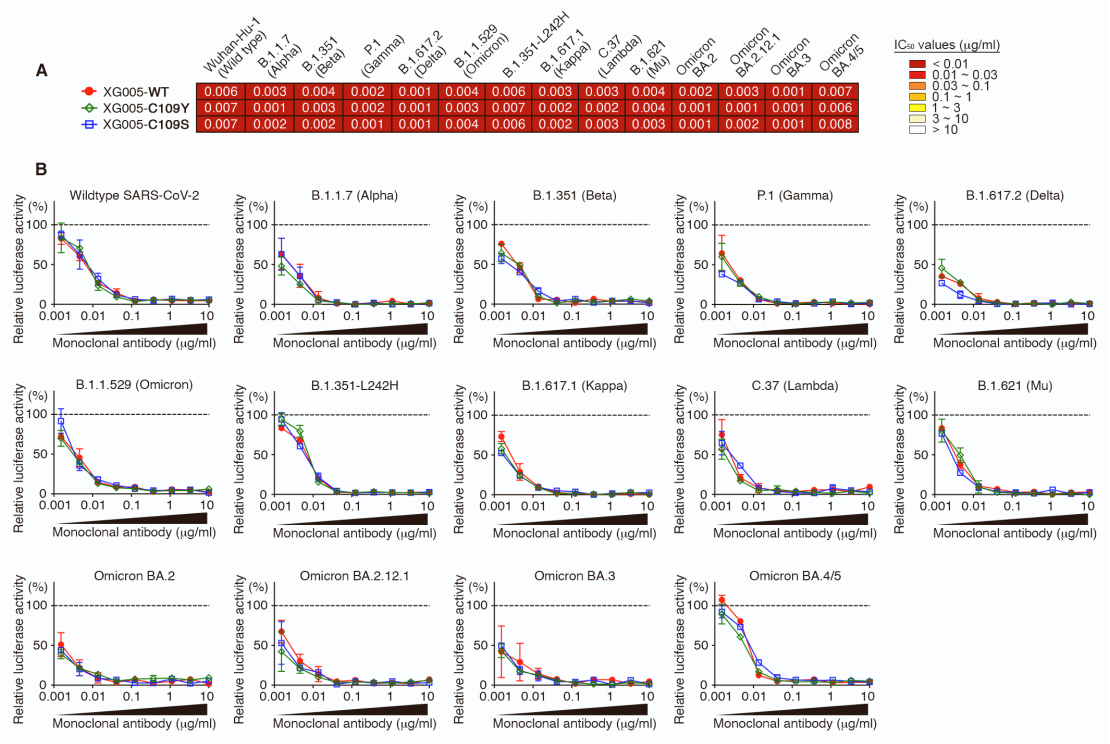

Figure S7. Engineered C109 variants of XG005 maintain neutralization potency. Related to Figure 7.

(A) IC_{50} values for XG005-WT, XG005-C109Y, and XG005-C109S measured against pseudoviruses of SARS-CoV-1, SARS-CoV-2 and its variants.

(B) Pseudovirus neutralization assays using different concentrations of XG005-WT, XG005-C109Y, and XG005-C109S. Mean of two independent experiments.

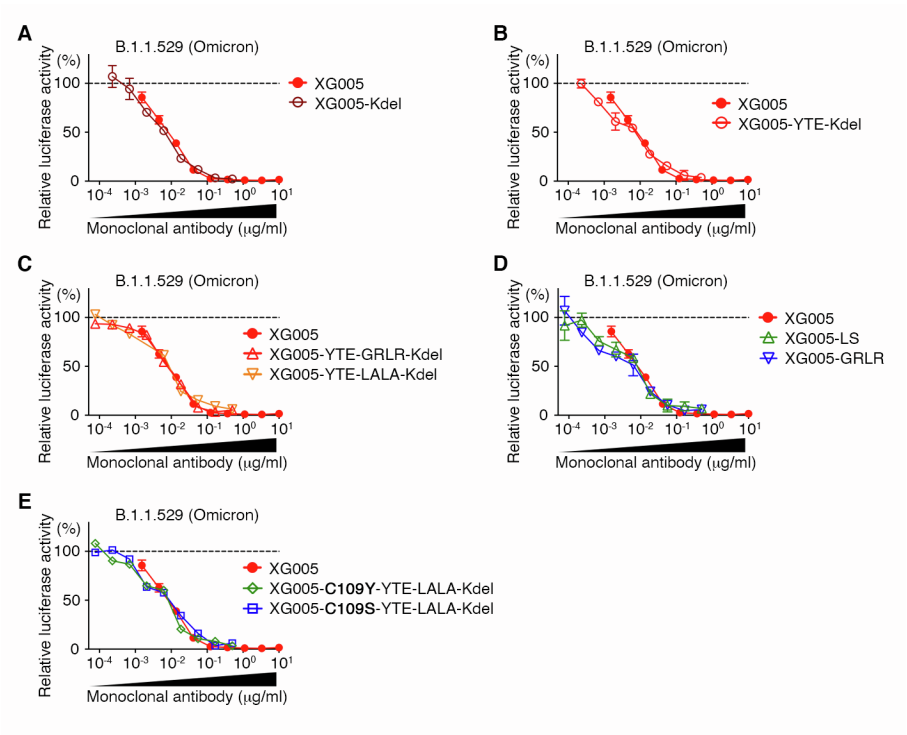

Figure S8. Engineered Fc variants of XG005 maintain neutralization potency. Related to Figure 7.

(A-D) Various engineered Fc variants of XG005 maintain the in vitro neutralizing activities against B.1.1.529 (Omicron) pseudoviruses. Kdel: mAb mutant with the deletion of heavy chain C-terminal lysine (A). YTE: mAb mutant with triple mutations M255Y, S257T and T259E in the Fc domain (B and C). LS: mAb mutant with M431L and N437S mutations in the Fc domain (D). Both YTE and LS substitutions result in an increase in its binding to human FcRn and a prolonged serum half-life of the antibody. GRLR: mAb mutant with G239R and L331R mutations in the Fc domain (C and D). LALA: mAb mutant with L237A and L238A mutations in the Fc domain (C). Both GRLR and LALA substitutions abrogate the antibody binding to FcγRs and eliminate the ADE effect.

Table S1. Cryo-EM data collection and refinement statistics of the Omicron S-XG005 complex. Related to Figure 3.

	State 1 (UDD with two Fabs)	State 2 (UDD with three Fabs)	State 3 (UDU with three Fabs)	RBD+Fab XG005
Data collection and processing				
Magnification	81,000			
Voltage (kV)	300			
Total dose (e^-/Å^2)	58			
Defocus range (μm)	-1.2 to -2.5			
Pixel size (Å)	1.064			
Symmetry imposed	C1			
Final particles (no.)	153,541	124,608	616,627	313,560
Map resolution (Å)	3.62	3.74	3.24	2.99
Refinement				
R.m.s. deviations				
Bond lengths (Å)	0.002	0.002	0.002	0.002
Bond angles (°)	0.558	0.509	0.517	0.479
Validation				
MolProbity score	2.40	2.24	2.23	2.46
Clashscore	7.16	5.99	6.11	6.30
Rotamer outlier (%)	5.83	4.53	4.85	5.46
Ramachandran plot				
Favored (%)	93.64	93.72	94.54	90.05
Allowed (%)	6.36	6.28	5.44	9.95
Disallowed (%)	0.00	0.00	0.00	0.00
EMDB	EMD-33744	EMD-33742	EMD-33743	EMD-33745
PDB	7YD0	7YCY	7YCZ	7YD1

Table S2. Amino acid sequences of the S protein of various pseudotyped viruses used for in vitro neutralization assays. Related to STAR Methods.

	Amino acid sequences of S protein	Mutation sites
SARS-CoV-1	MFIFLLFLTLTSGSDLDRCTTFDDVQAPNYTQHTSSMRGVYYPDEIFRSDTLYLTQDLFLPFYSNVTGFHTINHTFGNPVIPFKDGIYFAATEKSNVVRGWVFGSTMNNKSQSVIIINNSTNVVIRA CNFELCDNPFFAVSKPMGTQTHTMIFDNAFNCTFEYISDAFSLDVSEKSGNFKHLREFVFKNKDGFLYVYKGYQPIDVVRDLPSGFNTLKPIFKLPLGINITNFRAILTAFSPAQDIWGTSAAAYF VGYLKPTTFMLKYDENGTITDAVDCSQNPLAELKCSVKSFEIDKGIYQTSNFRVVPSGDVVRFPNITNLCPFGEVFNATKFPSVYAWERKKISNCVADYSVLYNSTFFSTFKCYGVSATKLNDLC FSNVYADSFVVKGDDVRQIAPGQTGVIADYNYKLPDDFMGCVLAWNTRNIDATSTGNYNYKYRYLRHGKLRPFERDISNVPFSPDGKPCTPPALNCYWPLNDYGFYTTTGIGYQPYRVVVLS FELLNAPATVCGPKLSTDLIKNQCVNFNFNGLTGTGVLTPSSKRFQPFQQFGRDVSDFTDSVRDPKTSEILDISPCSFGGVSVITPGTNASSEVAVLYQDVNCTDVSTAIHADQLTPAWRIYSTG NNVFQTQAGCLIGAEHVDTSYECDIPIGAGICASYHTVSLLRSTSQKSIVAYTMSLGADSSIAYSNNTIAIPTNFSISITTEVMPVSMAKTSVDCNMYICGDSTECANLLLQYGSFCTQLNRALSGI AAEQDRNTREVFAQVKQMYKTPTLKYFGGFNFSQILPDPLKPTKRSFIEDLLFNKVTLADAGFMKQYGECLGDINARDLICAQKFNGLTVLPPLLTDDMIAAYTAALVSGTATAGWTFGAGAAL QIPFAMQMAYRFNGIGVTQNVLYENQKQIANQFNKAISQIQESLTTTSTALGKLQDVVNQNAQALNTLVKQLSSNFGAISSVLNDILSRLDKVEAEVQIDRLITGRLQSLQTYVTQQLIRAAEIRAS ANLAATKMSECVLGQSKRVDFCGKGYHLMSFPQAAPHGVVFLHVTYVPSQERNFTTAPAICHEGKAYFPREGVFVFNGTSWFITQRNFFSPQIITTDNTFVSGNCDVVIGIINNTVYDPLQPEL DSFKEELDKYFKNHTSPDVDLGDISGINASVVNIQKEIDRLNEVAKNLNESLIDLQELGKYEQYIKWPWYVWLGFIAGLIAIVMVTILLCCMTSCCSCLKGACSCGSCCKFDEDDSEPVLKGVKLH YT*	
SARS-CoV-2_WT	MFVFLVLLPLVSSQCVNLTTRTQLPPAYTNSFTRGVYYPDKVFRSSVLHSTQDLFLPFFSNVTWFHAIHVSGTNGTKRFDNPVLPFNDGVYFASTEKSNIIRGWIFGTTLDSKTQSLLIVNNATN VVIKVCEFQFCNDPFLGVYYHKNNKSWMESEFRVYSSANNCTFEYVSQPFLMDLEGKQGNFKNLREFVFKNIDGYFKIYSKHTPINLVRDLPQGFSALEPLVDLPIGINITRFQTLLALHRSYLTP GDSSSGWTAGAAAYYVGYLQPRTFLLKYNENGTITDAVDCALDPLSETKCTLKSFTVEKGIYQTSNFRVQPTESIVRFPNITNLCPFGEVFNATRFASVYAWNRKRISNCVADYSVLYNSASFS TFKCYGVSPTKLNDLCFTNVYADSFVIRGDEVRQIAPGQTGKIADYNYKLPDDFTGCVIAWNSNNLDSKVGGNYNYLYRLFRKSNLKPFERDISTEIYQAGSTPCNGVEGFNCYFPLQSYGFQP TNGVGYQPYRVVVLSFELLHAPATVCGPKKSTNLVKNKCVNFNFNGLTGTGVLTESNKKFLPFQQFGRDIADTTDAVRDPQTLEILDITPCSFGGVSVITPGTNTSNQVAVLYQDVNCTEVPVA IHADQLTPTWRVYSTGSNVFQTRAGCLIGAEHVNNSYECDIPIGAGICASYQTQTNSPRRARSVASQSIIAYTMSLGAENSVAYSNNSIAIPTNFTISVTTEILPVSMTKTSVDCTMYICGDSTECS NLLLQYGSFCTQLNRALTGIAVEQDKNTQEVFAQVKQIYKTPPIKDFGGFNFSQILPDPSKPSKRSFIEDLLFNKVTLADAGFIKQYGDCLGDIAARDLICAQKFNGLTVLPPLLTDEMIAQYTSAL LAGTITSGWTFGAGAALQIPFAMQMAYRFNGIGVTQNVLYENQKLIANQFNSAIGKIQDSLSSTASALGKLQDVVNQNAQALNTLVKQLSSNFGAISSVLNDILSRLDKVEAEVQIDRLITGRLQS LQTYVTQQLIRAAEIRASANLAATKMSECVLGQSKRVDFCGKGYHLMSFPQSAPHGVVFLHVTYVPAQEKNFTTAPAICHDGKAHFPREGVFVSNGTHWFVTQRNFYEPQIITTDNTFVSGNC DVVIGIVNNTVYDPLQPELDSFKEELDKYFKNHTSPDVDLGDISGINASVVNIQKEIDRLNEVAKNLNESLIDLQELGKYEQYIKWPWYIWLGFIAGLIAIVMVTIMLCCMTSCCSCLKGCCSCGSC CKFDEDDSEPVLKGVKLHYT*	
B.1.1.7 (Alpha)	MFVFLVLLPLVSSQCVNLTTRTQLPPAYTNSFTRGVYYPDKVFRSSVLHSTQDLFLPFFSNVTWFHAISGTNGTKRFDNPVLPFNDGVYFASTEKSNIIRGWIFGTTLDSKTQSLLIVNNATNVVI KVCEFQFCNDPFLGVYHKNNKSWMESEFRVYSSANNCTFEYVSQPFLMDLEGKQGNFKNLREFVFKNIDGYFKIYSKHTPINLVRDLPQGFSALEPLVDLPIGINITRFQTLLALHRSYLTPGDS SSGWTAGAAAYYVGYLQPRTFLLKYNENGTITDAVDCALDPLSETKCTLKSFTVEKGIYQTSNFRVQPTESIVRFPNITNLCPFGEVFNATRFASVYAWNRKRISNCVADYSVLYNSASFSTFK CYGVSPTKLNDLCFTNVYADSFVIRGDEVRQIAPGQTGKIADYNYKLPDDFTGCVIAWNSNNLDSKVGGNYNYLYRLFRKSNLKPFERDISTEIYQAGSTPCNGVEGFNCYFPLQSYGFQPTY GVGYQPYRVVVLSFELLHAPATVCGPKKSTNLVKNKCVNFNFNGLTGTGVLTESNKKFLPFQQFGRDIADTTDAVRDPQTLEILDITPCSFGGVSVITPGTNTSNQVAVLYQGVNCTEVPVAIH ADQLTPTWRVYSTGSNVFQTRAGCLIGAEHVNNSYECDIPIGAGICASYQTQTNSHRRARSVASQSIIAYTMSLGAENSVAYSNNSIAIPINFTISVTTEILPVSMTKTSVDCTMYICGDSTECSNL LLQYGSFCTQLNRALTGIAVEQDKNTQEVFAQVKQIYKTPPIKDFGGFNFSQILPDPSKPSKRSFIEDLLFNKVTLADAGFIKQYGDCLGDIAARDLICAQKFNGLTVLPPLLTDEMIAQYTSALLA GTITSGWTFGAGAALQIPFAMQMAYRFNGIGVTQNVLYENQKLIANQFNSAIGKIQDSLSSTASALGKLQDVVNQNAQALNTLVKQLSSNFGAISSVLNDILSRLDKVEAEVQIDRLITGRLQSLQ TYVTQQLIRAAEIRASANLAATKMSECVLGQSKRVDFCGKGYHLMSFPQSAPHGVVFLHVTYVPAQEKNFTTAPAICHDGKAHFPREGVFVSNGTHWFVTQRNFYEPQIITTNNTFVSGNCDV VIGIVNNTVYDPLQPELDSFKEELDKYFKNHTSPDVDLGDISGINASVVNIQKEIDRLNEVAKNLNESLIDLQELGKYEQYIKWPWYIWLGFIAGLIAIVMVTIMLCCMTSCCSCLKGCCSCGSCCK FDEDDSEPVLKGVKLHYT*	del69-70, delY144, N501Y, A570D, D614G, P681H, T716I, S982A, D1118H
B.1.351-L242H	MFVFLVLLPLVSSQCVNFTTRTQLPPAYTNSFTRGVYYPDKVFRSSVLHSTQDLFLPFFSNVTWFHAIHVSGTNGTKRFANPVLPFNDGVYFASTEKSNIIRGWIFGTTLDSKTQSLLIVNNATN VVIKVCEFQFCNDPFLGVYYHKNNKSWMESEFRVYSSANNCTFEYVSQPFLMDLEGKQGNFKNLREFVFKNIDGYFKIYSKHTPINLVRGLPQGFSALEPLVDLPIGINITRFQTLHALHISYLTP GDSSSGWTAGAAAYYVGYLQPRTFLLKYNENGTITDAVDCALDPLSETKCTLKSFTVEKGIYQTSNFRVQPTESIVRFPNITNLCPFGEVFNATRFASVYAWNRKRISNCVADYSVLYNSASFS TFKCYGVSPTKLNDLCFTNVYADSFVIRGDEVRQIAPGQTGNIADYNYKLPDDFTGCVIAWNSNNLDSKVGGNYNYLYRLFRKSNLKPFERDISTEIYQAGSTPCNGVKGFNCYFPLQSYGFQ PTYGVGYQPYRVVVLSFELLHAPATVCGPKKSTNLVKNKCVNFNFNGLTGTGVLTESNKKFLPFQQFGRDIADTTDAVRDPQTLEILDITPCSFGGVSVITPGTNTSNQVAVLYQGVNCTEVPV AIHADQLTPTWRVYSTGSNVFQTRAGCLIGAEHVNNSYECDIPIGAGICASYQTQTNSPRRARSVASQSIIAYTMSLGVENSVAYSNNSIAIPTNFTISVTTEILPVSMTKTSVDCTMYICGDSTEC SNLLLQYGSFCTQLNRALTGIAVEQDKNTQEVFAQVKQIYKTPPIKDFGGFNFSQILPDPSKPSKRSFIEDLLFNKVTLADAGFIKQYGDCLGDIAARDLICAQKFNGLTVLPPLLTDEMIAQYTSA LLAGTITSGWTFGAGAALQIPFAMQMAYRFNGIGVTQNVLYENQKLIANQFNSAIGKIQDSLSSTASALGKLQDVVNQNAQALNTLVKQLSSNFGAISSVLNDILSRLDKVEAEVQIDRLITGRLQ SLQTYVTQQLIRAAEIRASANLAATKMSECVLGQSKRVDFCGKGYHLMSFPQSAPHGVVFLHVTYVPAQEKNFTTAPAICHDGKAHFPREGVFVSNGTHWFVTQRNFYEPQIITTDNTFVSGN CDVVIGIVNNTVYDPLQPELDSFKEELDKYFKNHTSPDVDLGDISGINASVVNIQKEIDRLNEVAKNLNESLIDLQELGKYEQYIKWPWYIWLGFIAGLIAIVMVTIMLCCMTSCCSCLKGCCSCGS CCKFDEDDSEPVLKGVKLHYT*	L18F, D80A, D215G, L242H, R246I, K417N, E484K, N501Y, D614G and A701V
B.1.351 (Beta)	MFVFLVLLPLVSSQCVNFTTRTQLPPAYTNSFTRGVYYPDKVFRSSVLHSTQDLFLPFFSNVTWFHAIHVSGTNGTKRFANPVLPFNDGVYFASTEKSNIIRGWIFGTTLDSKTQSLLIVNNATN VVIKVCEFQFCNDPFLGVYYHKNNKSWMESEFRVYSSANNCTFEYVSQPFLMDLEGKQGNFKNLREFVFKNIDGYFKIYSKHTPINLVRGLPQGFSALEPLVDLPIGINITRFQTLHISYLTPGDS SSGWTAGAAAYYVGYLQPRTFLLKYNENGTITDAVDCALDPLSETKCTLKSFTVEKGIYQTSNFRVQPTESIVRFPNITNLCPFGEVFNATRFASVYAWNRKRISNCVADYSVLYNSASFSTFK CYGVSPTKLNDLCFTNVYADSFVIRGDEVRQIAPGQTGNIADYNYKLPDDFTGCVIAWNSNNLDSKVGGNYNYLYRLFRKSNLKPFERDISTEIYQAGSTPCNGVKGFNCYFPLQSYGFQPTY GVGYQPYRVVVLSFELLHAPATVCGPKKSTNLVKNKCVNFNFNGLTGTGVLTESNKKFLPFQQFGRDIADTTDAVRDPQTLEILDITPCSFGGVSVITPGTNTSNQVAVLYQGVNCTEVPV AIHADQLTPTWRVYSTGSNVFQTRAGCLIGAEHVNNSYECDIPIGAGICASYQTQTNSPRRARSVASQSIIAYTMSLGVENSVAYSNNSIAIPTNFTISVTTEILPVSMTKTSVDCTMYICGDSTEC SNLLLQYGSFCTQLNRALTGIAVEQDKNTQEVFAQVKQIYKTPPIKDFGGFNFSQILPDPSKPSKRSFIEDLLFNKVTLADAGFIKQYGDCLGDIAARDLICAQKFNGLTVLPPLLTDEMIAQYTSALL AGTITSGWTFGAGAALQIPFAMQMAYRFNGIGVTQNVLYENQKLIANQFNSAIGKIQDSLSSTASALGKLQDVVNQNAQALNTLVKQLSSNFGAISSVLNDILSRLDKVEAEVQIDRLITGRLQSL QTYVTQQLIRAAEIRASANLAATKMSECVLGQSKRVDFCGKGYHLMSFPQSAPHGVVFLHVTYVPAQEKNFTTAPAICHDGKAHFPREGVFVSNGTHWFVTQRNFYEPQIITTDNTFVSGNCD VVIGIVNNTVYDPLQPELDSFKEELDKYFKNHTSPDVDLGDISGINASVVNIQKEIDRLNEVAKNLNESLIDLQELGKYEQYIKWPWYIWLGFIAGLIAIVMVTIMLCCMTSCCSCLKGCCSCGSCC KFDEDDSEPVLKGVKLHYT*	L18F, D80A, D215G, del242-244, R246I, K417N, E484K, N501Y, D614G and A701V
P.1 (Gamma)	MFVFLVLLPLVSSQCVNFTNRTQLPSAYTNSFTRGVYYPDKVFRSSVLHSTQDLFLPFFSNVTWFHAIHVSGTNGTKRFDNPVLPFNDGVYFASTEKSNIIRGWIFGTTLDSKTQSLLIVNNATN VVIKVCEFQFCNYPFLGVYYHKNNKSWMESEFRVYSSANNCTFEYVSQPFLMDLEGKQGNFKNLSEFVFKNIDGYFKIYSKHTPINLVRDLPQGFSALEPLVDLPIGINITRFQTLLALHRSYLTP GDSSSGWTAGAAAYYVGYLQPRTFLLKYNENGTITDAVDCALDPLSETKCTLKSFTVEKGIYQTSNFRVQPTESIVRFPNITNLCPFGEVFNATRFASVYAWNRKRISNCVADYSVLYNSASFS TFKCYGVSPTKLNDLCFTNVYADSFVIRGDEVRQIAPGQTGTIADYNYKLPDDFTGCVIAWNSNNLDSKVGGNYNYLYRLFRKSNLKPFERDISTEIYQAGSTPCNGVKGFNCYFPLQSYGFQP TYGVGYQPYRVVVLSFELLHAPATVCGPKKSTNLVKNKCVNFNFNGLTGTGVLTESNKKFLPFQQFGRDIADTTDAVRDPQTLEILDITPCSFGGVSVITPGTNTSNQVAVLYQGVNCTEVPVA IHADQLTPTWRVYSTGSNVFQTRAGCLIGAEYVNNSYECDIPIGAGICASYQTQTNSPRRARSVASQSIIAYTMSLGAENSVAYSNNSIAIPTNFTISVTTEILPVSMTKTSVDCTMYICGDSTECS NLLLQYGSFCTQLNRALTGIAVEQDKNTQEVFAQVKQIYKTPPIKDFGGFNFSQILPDPSKPSKRSFIEDLLFNKVTLADAGFIKQYGDCLGDIAARDLICAQKFNGLTVLPPLLTDEMIAQYTSAL LAGTITSGWTFGAGAALQIPFAMQMAYRFNGIGVTQNVLYENQKLIANQFNSAIGKIQDSLSSTASALGKLQDVVNQNAQALNTLVKQLSSNFGAISSVLNDILSRLDKVEAEVQIDRLITGRLQS LQTYVTQQLIRAAEIRASANLAAIKMSECVLGQSKRVDFCGKGYHLMSFPQSAPHGVVFLHVTYVPAQEKNFTTAPAICHDGKAHFPREGVFVSNGTHWFVTQRNFYEPQIITTDNTFVSGNC DVVIGIVNNTVYDPLQPELDSFKEELDKYFKNHTSPDVDLGDISGINASVVNIQKEIDRLNEVAKNLNESLIDLQELGKYEQYIKWPWYIWLGFIAGLIAIVMVTIMLCCMTSCCSCLKGCCSCGSC CKFDEDDSEPVLKGVKLHYT*	L18F, T20N, P26S, D138Y, R190S, K417T, E484K, N501Y, D614G, H655Y, T1027I
B.1.617.1 (Kappa)	MFVFLVLLPLVSSQCVNLTTRTQLPPAYTNSFTRGVYYPDKVFRSSVLHSTQDLFLPFFSNVTWFHAIHVSGTNGTKRFDNPVLPFNDGVYFASTEKSNIIRGWIFGTTLDSKTQSLLIVNNATN VVIKVCEFQFCNDPFLDVYYHKNNKSWMKSEFRVYSSANNCTFEYVSQPFLMDLEGKQGNFKNLREFVFKNIDGYFKIYSKHTPINLVRDLPQGFSALEPLVDLPIGINITRFQTLLALHRSYLTP GDSSSGWTAGAAAYYVGYLQPRTFLLKYNENGTITDAVDCALDPLSETKCTLKSFTVEKGIYQTSNFRVQPTESIVRFPNITNLCPFGEVFNATRFASVYAWNRKRISNCVADYSVLYNSASFS TFKCYGVSPTKLNDLCFTNVYADSFVIRGDEVRQIAPGQTGKIADYNYKLPDDFTGCVIAWNSNNLDSKVGGNYNYRYRLFRKSNLKPFERDISTEIYQAGSTPCNGVQGFNCYFPLQSYGFQ PTNGVGYQPYRVVVLSFELLHAPATVCGPKKSTNLVKNKCVNFNFNGLTGTGVLTESNKKFLPFQQFGRDIADTTDAVRDPQTLEILDITPCSFGGVSVITPGTNTSNQVAVLYQGVNCTEVPV AIHADQLTPTWRVYSTGSNVFQTRAGCLIGAEHVNNSYECDIPIGAGICASYQTQTNSRRRARSVASQSIIAYTMSLGAENSVAYSNNSIAIPTNFTISVTTEILPVSMTKTSVDCTMYICGDSTEC SNLLLQYGSFCTQLNRALTGIAVEQDKNTQEVFAQVKQIYKTPPIKDFGGFNFSQILPDPSKPSKRSFIEDLLFNKVTLADAGFIKQYGDCLGDIAARDLICAQKFNGLTVLPPLLTDEMIAQYTSA LLAGTITSGWTFGAGAALQIPFAMQMAYRFNGIGVTQNVLYENQKLIANQFNSAIGKIQDSLSSTASALGKLQDVVNQNAQALNTLVKQLSSNFGAISSVLNDILSRLDKVEAEVQIDRLITGRLQ SLQTYVTQQLIRAAEIRASANLAATKMSECVLGQSKRVDFCGKGYHLMSFPQSAPHGVVFLHVTYVPAHEKNFTTAPAICHDGKAHFPREGVFVSNGTDWFVTQRNFYEPQIITTDNTFVSGN CDVVIGIVNNTVYDPLQPELDSFKEELDKYFKNHTSPDVDLGDISGINASVVNIQKEIDRLNEVAKNLNESLIDLQELGKYEQYIKWPWYIWLGFIAGLIAIVMVTIMLCCMTSCCSCLKGCCSCGS CCKFDEDDSEPVLKGVKLHYT*	D111D, G142D, E154K, L452R, E484Q, D614G, P681R, Q1071H, H1101D

B.1.617.2 (Delta)	MFVFLVLLPLVSSQCVNLRTRTQLPPAYTNSFTRGVYYPDKVFRSSVLHSTQDLFLPFFSNVTWFHAIHVSGTNGTKRFDNPVLPFNDGVYFASTEKSNIIRGWIFGTTLDSKTQSLLIVNNATN VVIKVCEFQFCNDPFLDVYYHKNNKSWMESGVYSSANNCTFEYVSQPFLMDLEGKQGNFKNLREFVFKNIDGYFKIYSKHTPINLVRDLPQGFSALEPLVDLPIGINITRFQTLLALHRSYLTPG DSSSGWTAGAAAYYVGYLQPRTFLLKYNENGTITDAVDCALDPLSETKCTLKSFTVEKGIYQTSNFRVQPTESIVRFPNITNLCPFGEVFNATRFASVYAWNRKRISNCVADYSVLYNSASFST FKCYGVSPTKLNDLCFTNVYADSFVIRGDEVRQIAPGQTGKIADYNYKLPDDFTGCVIAWNSNNLDSKVGGNYNYRYRLFRKSNLKPFERDISTEIYQAGSKPCNGVEGFNCYFPLQSYGFQP TNGVGYQPYRVVVLSFELLHAPATVCGPKKSTNLVKNKCVNFNFNGLTGTGVLTESNKKFLPFQQFGRDIADTTDAVRDPQTLEILDITPCSFGGVSVITPGTNTSNQVAVLYQGVNCTEVPVA IHADQLTPTWRVYSTGSNVFQTRAGCLIGAEHVNNSYECDIPIGAGICASYQTQTNSRRRARSVASQSIIAYTMSLGAENSVAYSNNSIAIPTNFTISVTTEILPVSMTKTSVDCTMYICGDSTECS NLLLQYGSFCTQLNRALTGIAVEQDKNTQEVFAQVKQIYKTPPIKDFGGFNFSQILPDPSKPSKRSFIEDLLFNKVTLADAGFIKQYGDCLGDIAARDLICAQKFNGLTVLPPLLTDEMIAQYTSAL LAGTITSGWTFGAGAALQIPFAMQMAYRFNGIGVTQNVLYENQKLIANQFNSAIGKIQDSLSSTASALGKLQNVVNQNAQALNTLVKQLSSNFGAISSVLNDILSRLDKVEAEVQIDRLITGRLQS LQTYVTQQLIRAAEIRASANLAATKMSECVLGQSKRVDFCGKGYHLMSFPQSAPHGVVFLHVTYVPAQEKNFTTAPAICHDGKAHFPREGVFVSNGTHWFVTQRNFYEPQIITTDNTFVSGNC DVVIGIVNNTVYDPLQPELDSFKEELDKYFKNHTSPDVDLGDISGINASVVNIQKEIDRLNEVAKNLNESLIDLQELGKYEQYIKWPWYIWLGFIAGLIAIVMVTIMLCCMTSCCSCLKGCCSCGSC CKFDEDDSEPVLKGVKLHYT*	T19R, G142D, EFR156- 158G, L452R, T478K, D614G, P681R, D950N
C.37 (Lambda)	MFVFLVLLPLVSSQCVNLTTRTQLPPAYTNSFTRGVYYPDKVFRSSVLHSTQDLFLPFFSNVTWFHAIHVSGTNVIKRFDNPVLPFNDGVYFASTEKSNIIRGWIFGTTLDSKTQSLLIVNNATNV VIKVCEFQFCNDPFLGVYYHKNNKSWMESEFRVYSSANNCTFEYVSQPFLMDLEGKQGNFKNLREFVFKNIDGYFKIYSKHTPINLVRDLPQGFSALEPLVDLPIGINITRFQTLLALHNSSSGW TAGAAAYYVGYLQPRTFLLKYNENGTITDAVDCALDPLSETKCTLKSFTVEKGIYQTSNFRVQPTESIVRFPNITNLCPFGEVFNATRFASVYAWNRKRISNCVADYSVLYNSASFSTFKCYGVS PTKLNDLCFTNVYADSFVIRGDEVRQIAPGQTGKIADYNYKLPDDFTGCVIAWNSNNLDSKVGGNYNYQYRLFRKSNLKPFERDISTEIYQAGSTPCNGVEGFNCYSPLQSYGFQPTNGVGYQ PYRVVVLSFELLHAPATVCGPKKSTNLVKNKCVNFNFNGLTGTGVLTESNKKFLPFQQFGRDIADTTDAVRDPQTLEILDITPCSFGGVSVITPGTNTSNQVAVLYQGVNCTEVPVAIHADQLTP TWRVYSTGSNVFQTRAGCLIGAEHVNNSYECDIPIGAGICASYQTQTNSPRRARSVASQSIIAYTMSLGAENSVAYSNNSIAIPTNFTISVTTEILPVSMTKTSVDCTMYICGDSTECSNLLLQYG SFCTQLNRALTGIAVEQDKNTQEVFAQVKQIYKTPPIKDFGGFNFSQILPDPSKPSKRSFIEDLLFNKVTLADAGFIKQYGDCLGDIAARDLICAQKFNGLTVLPPLLTDEMIAQYTSALLAGTITS GWTFGAGAALQIPFAMQMAYRFNGIGVTQNVLYENQKLIANQFNSAIGKIQDSLSSTASALGKLQDVVNQNAQALNTLVKQLSSNFGAISSVLNDILSRLDKVEAEVQIDRLITGRLQSLQTYVT QQLIRAAEIRASANLAATKMSECVLGQSKRVDFCGKGYHLMSFPQSAPHGVVFLHVTYVPAQEKNFTTAPAICHDGKAHFPREGVFVSNGTHWFVTQRNFYEPQIITTDNTFVSGNCDVVIGIV NNTVYDPLQPELDSFKEELDKYFKNHTSPDVDLGDISGINASVVNIQKEIDRLNEVAKNLNESLIDLQELGKYEQYIKWPWYIWLGFIAGLIAIVMVTIMLCCMTSCCSCLKGCCSCGSCCKFDED DSEPVLKGVKLHYT*	G75V, T76I, RSYLTPGD246-253N, L452Q, F490S, D614G, T859N
B.1.621 (Mu)	MFVFLVLLPLVSSQCVNLTTRTQLPPAYTNSFTRGVYYPDKVFRSSVLHSTQDLFLPFFSNVTWFHAIHVSGTNGTKRFDNPVLPFNDGVYFASIEKSNIIRGWIFGTTLDSKTQSLLIVNNATNV VIKVCEFQFCNDPFLGVSNHKNNKSWMESEFRVYSSANNCTFEYVSQPFLMDLEGKQGNFKNLREFVFKNIDGYFKIYSKHTPINLVRDLPQGFSALEPLVDLPIGINITRFQTLLALHRSYLTP GDSSSGWTAGAAAYYVGYLQPRTFLLKYNENGTITDAVDCALDPLSETKCTLKSFTVEKGIYQTSNFRVQPTESIVRFPNITNLCPFGEVFNATKFASVYAWNRKRISNCVADYSVLYNSASFS TFKCYGVSPTKLNDLCFTNVYADSFVIRGDEVRQIAPGQTGKIADYNYKLPDDFTGCVIAWNSNNLDSKVGGNYNYLYRLFRKSNLKPFERDISTEIYQAGSTPCNGVKGFNCYFPLQSYGFQP TYGVGYQPYRVVVLSFELLHAPATVCGPKKSTNLVKNKCVNFNFNGLTGTGVLTESNKKFLPFQQFGRDIADTTDAVRDPQTLEILDITPCSFGGVSVITPGTNTSNQVAVLYQGVNCTEVPVA IHADQLTPTWRVYSTGSNVFQTRAGCLIGAEHVNNSYECDIPIGAGICASYQTQTNSHRRARSVASQSIIAYTMSLGAENSVAYSNNSIAIPTNFTISVTTEILPVSMTKTSVDCTMYICGDSTECSNLLL QLYGSFCTQLNRALTGIAVEQDKNTQEVFAQVKQIYKTPPIKDFGGFNFSQILPDPSKPSKRSFIEDLLFNKVTLADAGFIKQYGDCLGDIAARDLICAQKFNGLTVLPPLLTDEMIAQYTSALLAGT ITSGWTFGAGAALQIPFAMQMAYRFNGIGVTQNVLYENQKLIANQFNSAIGKIQDSLSSTASALGKLQNVVNQNAQALNTLVKQLSSNFGAISSVLNDILSRLDKVEAEVQIDRLITGRLQS LQTYVTQQLIRAAEIRASANLAATKMSECVLGQSKRVDFCGKGYHLMSFPQSAPHGVVFLHVTYVPAQEKNFTTAPAICHDGKAHFPREGVFVSNGTHWFVTQRNFYEPQIITTDNTFVSGNC DVVIGIVNNTVYDPLQPELDSFKEELDKYFKNHTSPDVDLGDISGINASVVNIQKEIDRLNEVAKNLNESLIDLQELGKYEQYIKWPWYIWLGFIAGLIAIVMVTIMLCCMTSCCSCLKGCCSCGSC CKFDEDDSEPVLKGVKLHYT*	T95I, Y144S, Y145N, R346K, E484K, N501Y, D614G, P681H, D950N
B.1.1.529 (Omicron)	MFVFLVLLPLVSSQCVNLTTRTQLPPAYTNSFTRGVYYPDKVFRSSVLHSTQDLFLPFFSNVTWFHVISGTNGTKRFDNPVLPFNDGVYFASIEKSNIIRGWIFGTTLDSKTQSLLIVNNATNVVIK VCEFQFCNDPFLDHKNNKSWMESEFRVYSSANNCTFEYVSQPFLMDLEGKQGNFKNLREFVFKNIDGYFKIYSKHTPIIVREPEDLPQGFSALEPLVDLPIGINITRFQTLLALHRSYLTPGDSS SGWTAGAAAYYVGYLQPRTFLLKYNENGTITDAVDCALDPLSETKCTLKSFTVEKGIYQTSNFRVQPTESIVRFPNITNLCPFDEVFNATRFASVYAWNRKRISNCVADYSVLYNLAPFFTFKCY GVSPTKLNDLCFTNVYADSFVIRGDEVRQIAPGQTGNIADYNYKLPDDFTGCVIAWNSNKLDSKVSGNYNYLYRLFRKSNLKPFERDISTEIYQAGNKPCNGVAGFNCYFPLRSYSFRPTYGV GHQPYRVVVLSFELLHAPATVCGPKKSTNLVKNKCVNFNFNGLKGTGVLTESNKKFLPFQQFGRDIADTTDAVRDPQTLEILDITPCSFGGVSVITPGTNTSNQVAVLYQGVNCTEVPVAIHAD QLTPTWRVYSTGSNVFQTRAGCLIGAEYVNNSYECDIPIGAGICASYQTQTKSHRRARSVASQSIIAYTMSLGAENSVAYSNNSIAIPTNFTISVTTEILPVSMTKTSVDCTMYICGDSTECSNLLL QYGSFCTQLKRALTGIAVEQDKNTQEVFAQVKQIYKTPPIKYFGGFNFSQILPDPSKPSKRSFIEDLLFNKVTLADAGFIKQYGDCLGDIAARDLICAQKFKGLTVLPPLLTDEMIAQYTSALLAGTI TSGWTFGAGAALQIPFAMQMAYRFNGIGVTQNVLYENQKLIANQFNSAIGKIQDSLSSTASALGKLQDVVNHNAQALNTLVKQLSSKFGAISSVLNDIFSRLDKVEAEVQIDRLITGRLQSLQTY VTQQLIRAAEIRASANLAATKMSECVLGQSKRVDFCGKGYHLMSFPQSAPHGVVFLHVTYVPAQEKNFTTAPAICHDGKAHFPREGVFVSNGTHWFVTQRNFYEPQIITTDNTFVSGNCDVVI GIVNNTVYDPLQPELDSFKEELDKYFKNHTSPDVDLGDISGINASVVNIQKEIDRLNEVAKNLNESLIDLQELGKYEQYIKWPWYIWLGFIAGLIAIVMVTIMLCCMTSCCSCLKGCCSCGSCCKF DEDDSEPVLKGVKLHYT*	A67V, del69-70, T95I, G142D/del143-145, del211/L212I, ins214EPE, G339D, S371L, S373P, S375F, K417N, N440K, G446S, S477N, T478K, E484A, Q493R, G496S, Q498R, N501Y, Y505H, T547K, D614G, H655Y, N679K, P681H, N764K, D796Y, N856K, Q954H, N969K, L981F
Omicron BA.1	MFVFLVLLPLVSSQCVNLTTRTQLPPAYTNSFTRGVYYPDKVFRSSVLHSTQDLFLPFFSNVTWFHVISGTNGTKRFDNPVLPFNDGVYFASIEKSNIIRGWIFGTTLDSKTQSLLIVNNATNVVIK VCEFQFCNDPFLDHKNNKSWMESEFRVYSSANNCTFEYVSQPFLMDLEGKQGNFKNLREFVFKNIDGYFKIYSKHTPIIVRDLPQGFSALEPLVDLPIGINITRFQTLLALHRSYLTPGDSSSGW TAGAAAYYVGYLQPRTFLLKYNENGTITDAVDCALDPLSETKCTLKSFTVEKGIYQTSNFRVQPTESIVRFPNITNLCPFDEVFNATRFASVYAWNRKRISNCVADYSVLYNLAPFFTFKCYGVS PTKLNDLCFTNVYADSFVIRGDEVRQIAPGQTGNIADYNYKLPDDFTGCVIAWNSNKLDSKVGGNYNYLYRLFRKSNLKPFERDISTEIYQAGNKPCNGVAGFNCYFPLRSYSFRPTYGVGHQ PYRVVVLSFELLHAPATVCGPKKSTNLVKNKCVNFNFNGLKGTGVLTESNKKFLPFQQFGRDIADTTDAVRDPQTLEILDITPCSFGGVSVITPGTNTSNQVAVLYQGVNCTEVPVAIHAD QLTPTWRVYSTGSNVFQTRAGCLIGAEYVNNSYECDIPIGAGICASYQTQTKSHRRARSVASQSIIAYTMSLGAENSVAYSNNSIAIPTNFTISVTTEILPVSMTKTSVDCTMYICGDSTECSNLLL QYGSFCTQLKRALTGIAVEQDKNTQEVFAQVKQIYKTPPIKYFGGFNFSQILPDPSKPSKRSFIEDLLFNKVTLADAGFIKQYGDCLGDIAARDLICAQKFKGLTVLPPLLTDEMIAQYTSALLAGTI TSGWTFGAGAALQIPFAMQMAYRFNGIGVTQNVLYENQKLIANQFNSAIGKIQDSLSSTASALGKLQDVVNHNAQALNTLVKQLSSKFGAISSVLNDIFSRLDKVEAEVQIDRLITGRLQSLQTYVTQ QLIRAAEIRASANLAATKMSECVLGQSKRVDFCGKGYHLMSFPQSAPHGVVFLHVTYVPAQEKNFTTAPAICHDGKAHFPREGVFVSNGTHWFVTQRNFYEPQIITTDNTFVSGNCDVVIGIVN NTVYDPLQPELDSFKEELDKYFKNHTSPDVDLGDISGINASVVNIQKEIDRLNEVAKNLNESLIDLQELGKYEQYIKWPWYIWLGFIAGLIAIVMVTIMLCCMTSCCSCLKGCCSCGSCCKFDEDD SEPVLKGVKLHYT*	A67V, del69-70, T95I, G142D/del143-145, del211/L212I, G339D, S371L, S373P, S375F, S477N, T478K, E484A, Q493R, G496S, Q498R, N501Y, Y505H, T547K, D614G, H655Y, N679K, P681H, N764K, D796Y, N856K, Q954H, N969K, L981F
Omicron BA.2	MFVFLVLLPLVSSQCVNLITRTQSYTNSFTRGVYYPDKVFRSSVLHSTQDLFLPFFSNVTWFHAIHVSGTNGTKRFDNPVLPFNDGVYFASTEKSNIIRGWIFGTTLDSKTQSLLIVNNATNVVIK VCEFQFCNDPFLDVYYHKNNKSWMESEFRVYSSANNCTFEYVSQPFLMDLEGKQGNFKNLREFVFKNIDGYFKIYSKHTPINLGRDLPQGFSALEPLVDLPIGINITRFQTLLALHRSYLTPGDS SSGWTAGAAAYYVGYLQPRTFLLKYNENGTITDAVDCALDPLSETKCTLKSFTVEKGIYQTSNFRVQPTESIVRFPNITNLCPFDEVFNATRFASVYAWNRKRISNCVADYSVLYNFAPFFAFKC YGVSPTKLNDLCFTNVYADSFVIRGNEVSQIAPGQTGNIADYNYKLPDDFTGCVIAWNSNKLDSKVGGNYNYLYRLFRKSNLKPFERDISTEIYQAGNKPCNGVAGFNCYFPLRSYGFRPTYG VGHQPYRVVVLSFELLHAPATVCGPKKSTNLVKNKCVNFNFNGLTGTGVLTESNKKFLPFQQFGRDIADTTDAVRDPQTLEILDITPCSFGGVSVITPGTNTSNQVAVLYQGVNCTEVPVAIHA DQLTPTWRVYSTGSNVFQTRAGCLIGAEYVNNSYECDIPIGAGICASYQTQTKSHRRARSVASQSIIAYTMSLGAENSVAYSNNSIAIPTNFTISVTTEILPVSMTKTSVDCTMYICGDSTECSNLL LQYGSFCTQLKRALTGIAVEQDKNTQEVFAQVKQIYKTPPIKYFGGFNFSQILPDPSKPSKRSFIEDLLFNKVTLADAGFIKQYGDCLGDIAARDLICAQKFNGLTVLPPLLTDEMIAQYTSALLAG TITSGWTFGAGAALQIPFAMQMAYRFNGIGVTQNVLYENQKLIANQFNSAIGKIQDSLSSTASALGKLQDVVNHNAQALNTLVKQLSSKFGAISSVLNDILSRLDKVEAEVQIDRLITGRLQSLQT YVTQQLIRAAEIRASANLAATKMSECVLGQSKRVDFCGKGYHLMSFPQSAPHGVVFLHVTYVPAQEKNFTTAPAICHDGKAHFPREGVFVSNGTHWFVTQRNFYEPQIITTDNTFVSGNCDVV IGIVNNTVYDPLQPELDSFKEELDKYFKNHTSPDVDLGDISGINASVVNIQKEIDRLNEVAKNLNESLIDLQELGKYEQYIKWPWYIWLGFIAGLIAIVMVTIMLCCMTSCCSCLKGCCSCGSCCKF DEDDSEPVLKGVKLHYT*	T19I, L24S, del25-27, G142D, V213G, G339D, S371F, S373P, S375F, T376A, D405N, R408S, K417N, N440K, S477N, T478K, E484A, Q493R, Q498R, N501Y, Y505H, D614G, H655Y, N679K, P681H, N764K, D796Y, Q954H, N969K
Omicron BA.2.12.1	MFVFLVLLPLVSSQCVNLITRTQSYTNSFTRGVYYPDKVFRSSVLHSTQDLFLPFFSNVTWFHAIHVSGTNGTKRFDNPVLPFNDGVYFASTEKSNIIRGWIFGTTLDSKTQSLLIVNNATNVVIK VCEFQFCNDPFLDVYYHKNNKSWMESEFRVYSSANNCTFEYVSQPFLMDLEGKQGNFKNLREFVFKNIDGYFKIYSKHTPINLGRDLPQGFSALEPLVDLPIGINITRFQTLLALHRSYLTPGDS SSGWTAGAAAYYVGYLQPRTFLLKYNENGTITDAVDCALDPLSETKCTLKSFTVEKGIYQTSNFRVQPTESIVRFPNITNLCPFDEVFNATRFASVYAWNRKRISNCVADYSVLYNFAPFFAFKC YGVSPTKLNDLCFTNVYADSFVIRGNEVSQIAPGQTGNIADYNYKLPDDFTGCVIAWNSNKLDSKVGGNYNYQYRLFRKSNLKPFERDISTEIYQAGNKPCNGVAGFNCYFPLRSYGFRPTYG VGHQPYRVVVLSFELLHAPATVCGPKKSTNLVKNKCVNFNFNGLTGTGVLTESNKKFLPFQQFGRDIADTTDAVRDPQTLEILDITPCSFGGVSVITPGTNTSNQVAVLYQGVNCTEVPVAIHA DQLTPTWRVYSTGSNVFQTRAGCLIGAEYVNNSYECDIPIGAGICASYQTQTKSHRRARSVASQSIIAYTMSLGAENLVAYSNNSIAIPTNFTISVTTEILPVSMTKTSVDCTMYICGDSTECSNLL LQYGSFCTQLKRALTGIAVEQDKNTQEVFAQVKQIYKTPPIKYFGGFNFSQILPDPSKPSKRSFIEDLLFNKVTLADAGFIKQYGDCLGDIAARDLICAQKFNGLTVLPPLLTDEMIAQYTSALLAG TITSGWTFGAGAALQIPFAMQMAYRFNGIGVTQNVLYENQKLIANQFNSAIGKIQDSLSSTASALGKLQDVVNHNAQALNTLVKQLSSKFGAISSVLNDILSRLDKVEAEVQIDRLITGRLQSLQT YVTQQLIRAAEIRASANLAATKMSECVLGQSKRVDFCGKGYHLMSFPQSAPHGVVFLHVTYVPAQEKNFTTAPAICHDGKAHFPREGVFVSNGTHWFVTQRNFYEPQIITTDNTFVSGNCDVV IGIVNNTVYDPLQPELDSFKEELDKYFKNHTSPDVDLGDISGINASVVNIQKEIDRLNEVAKNLNESLIDLQELGKYEQYIKWPWYIWLGFIAGLIAIVMVTIMLCCMTSCCSCLKGCCSCGSCCKF DEDDSEPVLKGVKLHYT*	T19I, L24S, del25-27, G142D, V213G, G339D, S371F, S373P, S375F, T376A, D405N, R408S, K417N, N440K, L452Q, S477N, T478K, E484A, Q493R, Q498R, N501Y, Y505H, D614G, H655Y, N679K, P681H, S704L, N764K, D796Y, Q954H, N969K

Omicron BA.3	MFVFLVLLPLVSSQCVNLTTRTQLPPAYTNSFTRGVYYPDKVFRSSVLHSTQDLFLPFFSNVTWFHVISGTNGTKRFDNPVLPFNDGVYFASIEKSNIIRGWIFGTTLDSKTQSLLIVNNATNVVIK VCEFQFCNDPFLDHKNNKSWMESEFRVYSSANNCTFEYVSQPFLMDLEGKQGNFKNLREFVFKNIDGYFKIYSKHTPIIVRDLPQGFSALEPLVDLPIGINITRFQTLLALHRSYLTPGDSSSGW TAGAAAYYVGYLQPRTFLLKYNENGTITDAVDCALDPLSETKCTLKSFTVEKGIYQTSNFRVQPTESIVRFPNITNLCPFDEVFNATRFASVYAWNRKRISNCVADYSVLYNFAPFFAFKCYGVS PTKLNDLCFTNVYADSFVIRGNEVSQIAPGQTGNIADYNYKLPDDFTGCVIAWNSNKLDSKVSGNYNYLYRLFRKSNLKPFERDISTEIYQAGNKPCNGVAGFNCYFPLRSYGFRPTYGVGHQ PYRVVVLSFELLHAPATVCGPKKSTNLVKNKCVNFNFNGLTGTGVLTESNKKFLPFQQFGRDIADTTDAVRDPQTLEILDITPCSFGGVSVITPGTNTSNQVAVLYQGVNCTEVPVAIHADQ LTPTWRVYSTGSNVFQTRAGCLIGAEYVNNSYECDIPIGAGICASYQTQTKSHRRARSVASQSIIAYTMSLGAENSVAYSNNSIAIPTNFTISVTTEILPVSMTKTSVDCTMYICGDSTECSNLLLQ YGSFCTQLKRALTGIAVEQDKNTQEVFAQVKQIYKTPPIKYFGGFNFSQILPDPSKPSKRSFIEDLLFNKVTLADAGFIKQYGDCLGDIAARDLICAQKFNGLTVLPPLLTDEMIAQYTSALLAGTIT SGWTFGAGAALQIPFAMQMAYRFNGIGVTQNVLYENQKLIANQFNSAIGKIQDSLSSTASALGKLQDVVNHNAQALNTLVKQLSSKFGAISSVLNDILSRLDKVEAEVQIDRLITGRLQSLQTYVT QQLIRAAEIRASANLAATKMSECVLGQSKRVDFCGKGYHLMSFPQSAPHGVVFLHVTYVPAQEKNFTTAPAICHDGKAHFPREGVFVSNGTHWFVTQRNFYEPQIITTDNTFVSGNCDVVIGIV NNTVYDPLQPELDSFKEELDKYFKNHTSPDVDLGDISGINASVVNIQKEIDRLNEVAKNLNESLIDLQELGKYEQYIKWPWYIWLGFIAGLIAIVMVTIMLCCMTSCCSCLKGCCSCGSCCKFDED DSEPVLKGVKLHYT*	A67V, del69-70, T95I, G142D, del143-145, del211/L212I, G339D, S371F, S373P, S375F, T376A, D405N, R408S, K417N, N440K, G446S, S477N, T478K, E484A, Q493R, Q498R, N501Y, Y505H, D614G, H655Y, N679K, P681H, N764K, D796Y, Q954H, N969K
Omicron BA.4/5	MFVFLVLLPLVSSQCVNLITRTQSYTNSFTRGVYYPDKVFRSSVLHSTQDLFLPFFSNVTWFHAISGTNGTKRFDNPVLPFNDGVYFASTEKSNIIRGWIFGTTLDSKTQSLLIVNNATNVVIKVC EFQFCNDPFLDVYYHKNNKSWMESEFRVYSSANNCTFEYVSQPFLMDLEGKQGNFKNLREFVFKNIDGYFKIYSKHTPINLGRDLPQGFSALEPLVDLPIGINITRFQTLLALHRSYLTPGDSSS GWTAGAAAYYVGYLQPRTFLLKYNENGTITDAVDCALDPLSETKCTLKSFTVEKGIYQTSNFRVQPTESIVRFPNITNLCPFDEVFNATRFASVYAWNRKRISNCVADYSVLYNFAPFFAFKCYG VSPTKLNDLCFTNVYADSFVIRGNEVSQIAPGQTGNIADYNYKLPDDFTGCVIAWNSNKLDSKVGGNYNYRYRLFRKSNLKPFERDISTEIYQAGNKPCNGVAGVNCYFPLQSYGFRPTYGVG HQPYRVVVLSFELLHAPATVCGPKKSTNLVKNKCVNFNFNGLTGTGVLTESNKKFLPFQQFGRDIADTTDAVRDPQTLEILDITPCSFGGVSVITPGTNTSNQVAVLYQGVNCTEVPVAIHADQ LTPTWRVYSTGSNVFQTRAGCLIGAEYVNNSYECDIPIGAGICASYQTQTKSHRRARSVASQSIIAYTMSLGAENSVAYSNNSIAIPTNFTISVTTEILPVSMTKTSVDCTMYICGDSTECSNLLLQ YGSFCTQLKRALTGIAVEQDKNTQEVFAQVKQIYKTPPIKYFGGFNFSQILPDPSKPSKRSFIEDLLFNKVTLADAGFIKQYGDCLGDIAARDLICAQKFNGLTVLPPLLTDEMIAQYTSALLAGTIT SGWTFGAGAALQIPFAMQMAYRFNGIGVTQNVLYENQKLIANQFNSAIGKIQDSLSSTASALGKLQDVVNHNAQALNTLVKQLSSKFGAISSVLNDILSRLDKVEAEVQIDRLITGRLQSLQTYVT QQLIRAAEIRASANLAATKMSECVLGQSKRVDFCGKGYHLMSFPQSAPHGVVFLHVTYVPAQEKNFTTAPAICHDGKAHFPREGVFVSNGTHWFVTQRNFYEPQIITTDNTFVSGNCDVVIGIV NNTVYDPLQPELDSFKEELDKYFKNHTSPDVDLGDISGINASVVNIQKEIDRLNEVAKNLNESLIDLQELGKYEQYIKWPWYIWLGFIAGLIAIVMVTIMLCCMTSCCSCLKGCCSCGSCCKFDED DSEPVLKGVKLHYT*	T19I, L24S, del25-27, del69-70, G142D, V213G, G339D, S371F, S373P, S375F, T376A, D405N, R408S, K417N, N440K, L452R, S477N, T478K, E484A, F486V, Q498R, N501Y, Y505H, D614G, H655Y, N679K, P681H, N764K, D796Y, Q954H, N969K